Additive Manufacturing of Functionally Graded Materials from Lunar Regolith

Final report

Authors: Vera Popovich[1], Mathilde Laot[1], Ina Cheibas[2], Belinda Rich[2]
Affiliation: [1]Delft University of Technology, [2]ESA ACT

Date: 09/12/2020

ACT research category: Space Architecture and Infrastructure (Habitats)

Contacts:

Vera Popovich
Tel: +31(0)152789568
e-mail: V.Popovich@tudelft.nl

Leopold Summerer (Technical Officer)
Tel: +31(0)715654192
Fax: +31(0)715658018
e-mail: act@esa.int

Available on the ACT website
http://www.esa.int/act

Ariadna ID: 19/9401
Ariadna study type: Standard
Contract Number: 4000128144/19/NL/AS

Table of Contents

1 Abstract 3
2 Introduction 4
2.1 In-Situ Resource Utilisation (ISRU) 4
2.2 Functionally Graded Materials 4
2.3 State of the Art 5
3 Materials and Methods 7
3.1 Powder Characterisation 7
3.1.1 Bulk chemistry and mineralogy 7
3.1.2 Particle size distribution 9
3.1.3 Particle shape 9
3.1.4 Bulk density 9
3.1.5 Thermal analysis 10
3.2 Additive Manufacturing Consolidation Techniques 11
3.2.1 Digital Light Processing 11
3.2.2 Spark Plasma Sintering 12
3.2.3 Laser Melting Additive Manufacturing 13
3.3 Microstructural and Morphological Characterisation 14
3.4 Simulation: Finite Element Method 14
4 Results and Discussion 16
4.1 Consolidation of Lunar Regolith 16
4.1.1 Digital Light Processing (DLP) 16
4.1.2 Spark Plasma Sintering (SPS) 17
4.2 Consolidation of Metallic Powders 22
4.3 Consolidation of Functionally Graded Material 25
4.3.1 FGM Composite of Regolith and Stainless Steel (316L) 25
4.3.2 FGM Composite of Regolith and Ti_6Al_4V Alloy 27
..... 28
4.4 Laser Scanning 27
4.5 Finite Element Method Simulation 31
5 Conclusions 34
5.1 Future Work 35
6 Acknowledgements 35
7 References 36

1 Abstract

This study aims to investigate the option to develop functionally graded materials (FGMs) with in-situ resources in view of their potential application for aerospace components and space habitats. The study aims to develop a composite at the level of concept validation by the selection and evaluation of suitable additive manufacturing (AM) techniques.

FGMs are high-performance composite materials, which offer advantages such as localized tailoring of material properties, improved interfacial boundary compatibility, and enhanced thermomechanical behaviour. Much of the current ISRU manufacturing research explores AM of as-received regolith, with some consideration given to metal alloys extracted in-situ. This study combines these two aspects by investigating the feasibility of in-situ manufactured metallic-regolith FGMs.

In the initial study phase, three regolith simulants (EAC-1A, LHS-1, LMS-1) were selected and characterised to assess their suitability for FGM manufacture and identify optimum processing conditions. An extensive review of current regolith consolidation technologies was also carried out and their compatibility with metallic-ceramic processing in a space environment was evaluated.

Two techniques, namely Digital Light Processing (DLP) and Spark Plasma Sintering (SPS), were selected for the second study phase. The chosen techniques were assessed on their capability to effectively consolidate regolith and metallic powders (stainless steel 316L and Ti_6Al_4V) separately, before progressing to manufacture of a functionally graded material. Laser scanning was also investigated as a method to deposit regolith layers onto metal substrate for application of FGM coatings. In parallel, a Finite Element Method simulation of the DLP sintering step was developed to model the effect of processing parameters on the sinter stresses.

While the current study showed that it is feasible to additively manufacture FGMs from lunar regolith, further developments of a fully optimized method have the potential to produce tailored, high-performance materials in an off-earth manufacturing setting, for the production of aerospace, robotic, or architectural components.

2 Introduction

2.1 In-Situ Resource Utilisation (ISRU)

Lunar explorations are an essential step for long-term space expeditions. The Moon is exceptionally advantageous compared to other planetary bodies because of its proximity and fastest communication to Earth [1]. It can serve as a strategic cornerstone of future technological developments in aerospace science and engineering, physics, and other disciplines [2]. Therefore, the lunar infrastructure is critical for a successful mission. Space habitats and engineering tools must ensure a high security and safety level against the harsh lunar environmental conditions, such as radiation, meteoroids, thermal fluctuations, and ultra-high vacuum [3][4]. Furthermore, the ideal infrastructure would be autonomous and with self-repair capabilities to substantially diminish the payload weight brought from Earth [5]. Thus, it is proposed to manufacture resilient and affordable human and robotic exploration tools using local resources.

In-situ Resource Utilization (ISRU) is a key and prominent strategy to manufacture space habitats and components [6][7]. The primary material for ISRU, and most abundant on the Moon, is regolith. Regolith is an abrasive and corrosive powder that contains several silicates (plagioclase, feldspar, pyroxene, olivine) and oxide minerals (ilmenite, spinel) [8][9]. This powder is also abundant in metals such as silicon, aluminium, iron, titanium, and magnesium [10]–[13]. The metals can be extracted by pyrometallurgy, electrometallurgy, and hydrometallurgy methods, with oxygen resulting as by-product in this refining process [14]–[16].

Much of the current research couples ISRU with Additive Manufacturing (AM) to build space habitats and engineering tools with regolith simulants [17]–[20]. However, the vast majority of such components have inadequate mechanical properties [21]. The material behaviour is limited in compressive or tensile strength and is not able to overcome the multitude of environmental space requirements [22]–[26]. Such environmental factors include solar energetic particles (SEP), galactic cosmic rays (GCR), abrasion, wear, thermal fluctuations, refrigeration, ultra-high vacuum, resistance to fatigue, impact and pressurization, meteoroids and mechanical impacts, and biological and chemical inertness [27]. Therefore, there is a need for resilient composites that can overcome all these environmental parameters.

2.2 Functionally Graded Materials

Functionally Graded Materials (FGMs) are high-performance composites designed to achieve tailored features [28]. They feature a graduated morphology, whereby different regions of a functionally graded composite exhibit different material composition, structure and/or behaviour. Examples of morphological gradients include material fraction, phase fraction, additive volume fraction, porosity, grain shape, grain size, and grain orientation – see Figure 1 [29][30][31]. Functionally graded layers can serve as an optimal transition between two incompatible materials; for example, a graded composition at a ceramic-metallic interface improves compatibility by promoting stronger bonding between substrates and preventing delamination, as well as reducing challenges related to interfacial mismatch such as fretting wear, fatigue, fracture, corrosion, and stress corrosion cracking [32][33]. Besides the benefit of improved mechanical behaviour, thermal properties can also be enhanced by a specific sequence of graded insulation layers [32][34].

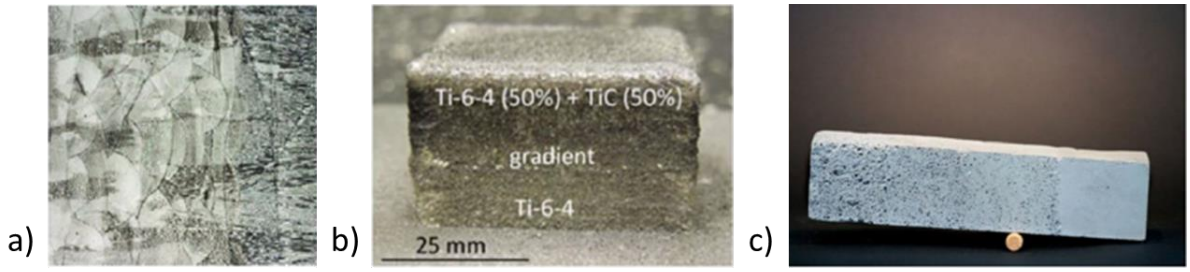

Figure 1. Schematic examples of functionally graded materials, characterized by the following morphology gradients: a) grain size/orientation [39], b) material fraction [112], c) porosity [113]

FGMs have the potential to overcome a multitude of lunar requirements with functions or performances embodied in a graduated morphology. They maximise ISRU capabilities due to their multi-material approach, evaluated as high performance contrary to monolithic applications [35]–[37]. In recent years, metal-ceramic gradients have been widely studied because of highly attractive properties, such as high-temperature stability, hardness, corrosion resistance, and good versatility [38]–[46]. Therefore, a regolith to metal gradient can be manufactured to secure ceramic-like properties transitioned to metal-like behaviour [41][42].

This research is focused on the feasibility of manufacturing a regolith-metallic FGM on the lunar surface with in-situ resources. On the lunar surface, the primary and most abundant resource for ISRU is regolith, which exists as a layer of unconsolidated mineral of depth 3 - 20m atop the lunar surface, with particle size ranging from fine dust to large rocks [49].
The lunar soil is abundant in metals such as silicon, aluminium, iron, titanium, and magnesium. Potential metal extraction methods from regolith include pyrometallurgy, electrometallurgy, and hydrometallurgy. In each discipline, the reduction of each component to its elemental form must have a process reactant that can be recycled indefinitely, be suited for lunar surface conditions, and consume minimal water [50]. Silicon, aluminium, and glass can be refined using fluorine, in a multi-stage reduction process that separates and purifies the elements. Oxygen is a by-product in this refining process, which is a high-priority resource for human life support or rocket fuel [15]. Molten salt electrolysis (Metalysis-FFC) technique has been tested on a lunar simulant JSA-2A to process metal alloys as products. The method produced three dominant distinct alloy groups, Al/Fe alloy, Fe/Si alloy (sometimes with the inclusion of Ti or Al), and Ca/Si/Al alloy (sometimes with the inclusion of Mg). Depending on the feedstock, Metalysis-FFC has the potential to produce specially-design alloys from refining of lunar regolith [51]. The extracted lunar resources that show potential for FGM application, and thus the ones considered in this study, include titanium, titanium alloys, iron (steel), magnesium, aluminium, and aluminium alloys. The primary criteria for material selection will be based on metal compatibility with regolith powder; this includes particle size distribution, particle shape density and thermal properties.

2.3 State of the Art

Current FGM fabrication methods can be classified as thin-film or bulk fabrication. Thin sections/coatings have the advantage of being less time consuming, for which fabrication processes such as physical/chemical vapour deposition are generally applied [52]. Bulk FGMs are more demanding and commonly use conventional powder metallurgical technologies [31][53]. In this study, which focuses on the application of FGMs for components or a space habitat, bulk manufacturing techniques that could be considered include material extrusion [54][55][56], light polymerisation [57], spark plasma sintering [58], powder bed [59][60][61] and powder fed techniques [62][63] [64].
The selection between additive manufacturing (AM) and conventional methods depends upon technique viability for processing both ceramic and metal/alloy powders, suitability for microgravity, and resultant mechanical post-fabrication properties. As a part of this research, an extensive literature

Table 1. Overview of advantages and disadvantages of consolidation techniques suitable for ISRU

Consolidation technique			Advantages	Disadvantages
Additive Manufacturing	Material Extrusion	**Sulfur Concrete** [65][55]	• Ease of manufacturing • Presence of FeS on the Moon • Cheap process	• Feasibility of S extraction from ores • Low impact resistance • Relatively high rate of S sublimation
	Power Bed Fusion	**Selective Laser Melting (SLM)** [66][67]	• Can produce high quality components in low to medium batch • Good repeatability • Full design flexibility • Low waste compared to conventional casting techniques (no machining) • Production of nearly fully dense parts	• Slow process and poor surface finish • Residual stresses (cracking) • Porosity (requires post-processing) • Lack of knowledge about the interaction between laser and ceramics • Powder sieving or crushing required • Powder heterogeneity causes variations in energy density
		Solar Sintering [59][19]	• Use of solar light source, more stable on the Moon • No need of binders	• Difficulty when sintered under vacuum • Low mechanical properties • Poor bonding between layers • Balancing sintered and molten phases • No prediction on the equipment lifetime • Few investigations carried out so far
	Binder Jetting	**D-shape Process** [22]	• Allows large-scale manufacturing in one single printing process • No need of sieving or crushing of the lunar regolith	• Large printer brought to the Moon • Use of an inorganic binder and an ink • Low shape accuracy • Multistep process lasting hours
	Photopoly-merization	**Stereo-lithography** [68][69]**/ Digital Light Processing (DPL)** [57][70]	• Good surface finish • More accurate and complex shape • Can produce small parts with high precision but also large parts whilst maintaining high precision • No mould required, only CAD	• Requires specific polymeric resins • Multistep and time demanding process • Expensive process • Difficult to achieve high density • Complex curing process • Needs smaller (nano scale) particle size
Conventional or hybrid fabrication	**Spark Plasma Sintering (SPS)** [71][58]		• Microstructure control due to low temperature and short time • High density due to higher heating rate and pressure • Dissimilar materials can be sintered • Fast and FGMs can be produced • Cost of SPS is 50 – 80% lower than other conventional techniques • Temperature of 900°C enough for sintering lunar regolith • Good mechanical properties	• Only simple symmetrical shapes can be prepared • Expensive DC generator required • For very small powders (less than 100 nm), significant temperature gradient can lead to non-uniform densification • Sieving or crushing required for lunar regolith • Limited to simple shapes
	Vacuum Sintering [72]		• Sintered parts with low thermal conductivity • Prevention of oxidization	• High weight loss increasing with temperature • Presence of macro-pores, which can be controlled with sintering temperature • Shrinkage dependent on the temperature

	Thermite reactions [73][74]	• Reduction of energy needed • Limited equipment is required • Quick reactions with smaller particles	• Addition of Al and other substances like Teflon • Porous structures • Little information about mechanical properties • Sieving or crushing required for lunar regolith • Deformation and surface cracking (even more with smaller particles)

review study was carried out to evaluate viable techniques for in-situ FGM manufacture: an overview of the different promising consolidation techniques suitable for ISRU, as well as their advantages and disadvantages, is given in Table 1. (For full literature review, the authors direct the reader to Annex 5 of this study)

The following methods are concluded to be most promising for FGM manufacture with regolith: (i) Spark Plasma Sintering (SPS) is selected due to the higher powder densification in the sintering technique, essential for building reliable structural components [33]; and (ii) Digital Light Processing (DLP) as this method works both with ceramic and metal powders whilst being suited to a microgravity environment [70].

3 Materials and Methods

3.1 Powder Characterisation

Three regolith simulants were evaluated for manufacture of a functionally-graded material: EAC-1A, LHS-1 (Lunar Highlands Simulant) and LMS-1 (Lunar Mare Simulant). Selection of these simulants is based on resemblance to Apollo sample bulk chemistry, and mineralogical diversity of the location (Mare and Highlands). EAC-1A simulant was sourced from the European Astronaut Centre, Cologne, Germany; LHS-1 and LMS-1 simulants were sourced from CLASS Exolith Lab, Orlando, USA [48][49].

3.1.1 Bulk chemistry and mineralogy

Use of simulant powders for the current study is necessary due to the limited availability of lunar soil. While Apollo missions and robotic lunar landers are the benchmark for simulant development, some differences between the terrestrial simulants and the actual lunar material are to be expected. Table 2 and Table 3 show that the oxide and mineralogical compositions of the chosen simulants can be considered comparable to Apollo lunar samples. Lunar Highlands soils are predominantly comprised of anorthosite, a rock which is largely made up of plagioclase feldspar. Lunar Mare soils contains volcanic rock that erupted at the lunar surface and produced lava flows and pyroclastic deposits [77]. Figure 2. XRD analysis of three regolith simulants: EAC-1A, LHS-1 and LMS-1 shows X-ray diffraction (XRD) patterns for all three lunar regolith simulants and confirms the presence of plagioclase, pyroxenes and iron oxide.

Table 2. Oxide composition (given in wt%) of three lunar regolith simulants (EAC-1A [114], LHS-1 [81], LMS-1 [82]) and the lunar Apollo samples from Mare and Highlands regions [77]

	EAC-1A	LHS-1	LMS-1	Apollo Mare	Apollo Highland
SiO_2	43.70	44.18	42.18	37.60	45.50
TiO_2	2.40	0.79	4.62	12.10	0.60
Al_2O_3	12.60	26.24	14.13	8.74	24.00
Cr_2O_3	-	0.02	0.21	0.42	-
Fe_2O_3	12.00	-	-	21.50	5.90
FeO_x	-	3.04	7.87	-	-
MgO	11.90	11.22	18.89	8.21	7.50
MnO	0.20	0.05	0.15	0.22	-
CaO	10.80	11.62	5.94	10.30	15.90
Na_2O	2.90	2.30	4.92	0.39	0.60
K_2O	1.30	0.46	0.57	0.08	-
SO_3	-	0.10	0.11	-	-
SrO	-	-	-	-	-
P_2O_5	0.60	-	-	0.05	-
Total	**98.40**	**100**	**99.56**	**99.58**	**100**

Table 3. Summary of mineralogical content (in wt.%) of three lunar regolith simulants (EAC-1A [115], LHS-1 [81] and LMS-1 [82]) in comparison to mineralogical data from Apollo 17 samples [116]. Note that Opaques is a mineral classification encapsulating oxides and sulphides, primarily ilmenite and iron oxide.

	EAC-1A	LHS-1	LMS-1	Apollo 17
Plagioclase	17.0	32.8	74.4	18.8
Glass	-	24.5	24.2	3.4
Basalt	-	19.8	0.5	-
Ilmenite	-	11.1	0.4	-
Pyroxene	22.0	7.5	0.3	44.6
Olivine	14.0	4.3	0.2	4.0
Iron Oxide	13.0	-	-	-
Opaques*	-	-	-	27.1
Other	8.0	-	-	1.4
Total	**74.0**	**100**	**100**	**99.3**

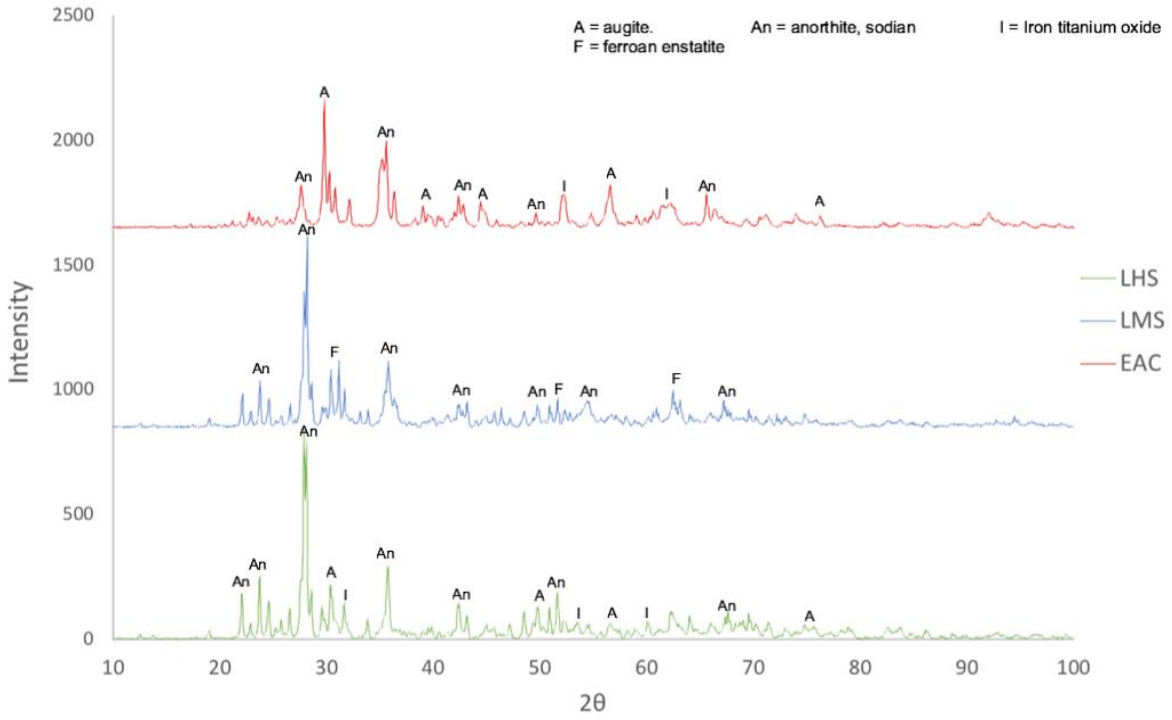

Figure 2. XRD analysis of three regolith simulants: EAC-1A, LHS-1 and LMS-1

3.1.2 Particle size distribution

Lunar regolith samples from Apollo missions were found to have log-normal size distribution with mean diameters typically between 45 µm and 100 µm, although particles can be as small as 10 nm [78][79]. The particle size distribution of the three simulants is given in Figure 3a. All simulants exhibit a wide particle size range, namely 0.02 µm - 2000 µm for EAC-1A and <1 µm - 1000 µm for LHS-1 and LMS-1. The mean particle size is 10.5 µm for EAC-1A, 94 µm for LHS-1 and 63 µm for LMS-1 [80]–[82]. All simulants display a significant fraction of large grains (>1mm), which is problematic for additive manufacturing.

Due to this, all three simulants underwent sieving through 50 or 100 µm mesh sieves to allow better sintering. Moreover, a 30g batch of EAC-1A was milled in a Retsch planetary ball mill in an argon atmosphere using tungsten carbide balls (5 and 10 mm). The powder was milled for 30 hours at a speed of 300 rpm with a ball to powder mass ratio of 10:1. The contamination was kept very low and the maximum particle size was reduced to 22 µm with mean particle size of 5 µm.

3.1.3 Particle shape

The particle shape has great influence over the flow and packing behaviour of powders, which affects in turn the properties of the consolidated material. Lunar particles are irregular in shape and have high cohesion in comparison to terrestrial materials, due to the environmental factors of the lunar surface; as a result, lunar regolith is highly abrasive (Figure 2 and Figure 3b-d) [83]. This abrasive property is difficult to simulate using Earth material, which should be considered during this feasibility study. From initial observations, LMS-1 and LHS-1 particles exhibit larger particle elongation and lower circularity than EAC-1A.

3.1.4 Bulk density

Most AM techniques involve the loose deposition of one material layer over another one. For this reason, poured bulk density was measured instead of tapped density. Poured density is useful in this study to determine the quantity of material required for the manufacturing process. Measurements on lunar soil samples, namely Apollo 14 and Apollo 15, have revealed bulk densities that vary from a minimum 0.87 g/cm^2 to a maximum 1.89 g/cm^2**.** The reason for

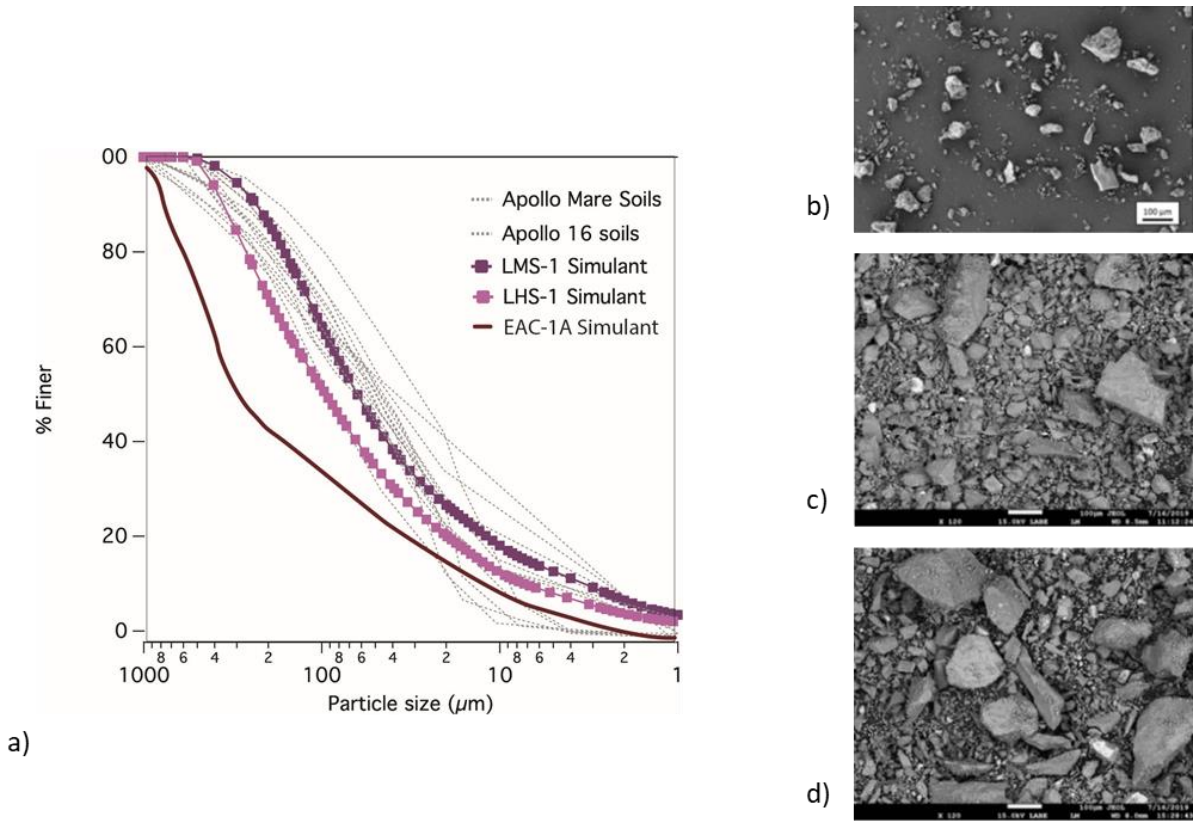

Figure 3. Simulant powder characterisation. a) Average particle size distribution for EAC-1A [117], LHS-1 [81] and LMS-1 [82]. Apollo data is shown for comparison, and has been adjusted to remove the >1mm fraction [81,82]. b)c)d) SEM images displaying as-received particle shape for b) EAC-1A [117], c) LHS-1 [81] and d) LMS-1 [82] simulants.

this variation is related to specific gravity, re-entrant intra-granular voids, particle shape, particle size distribution, and surface texture [84].

Poured bulk density was measured for simulants EAC-1A, LMS-1 and LHS-1 in accordance with ASTM D7481-18 (Standard Test Methods for Determining Loose and Tapped Bulk Densities of Powders using a Graduated Cylinder) [85]. 100 g of powder was poured into a 100 mL graduated cylinder and levelled; the density was calculated from the mass of the sample divided by the untapped volume occupied by the simulant. Three measurements were carried out per sample, with results derived from the mean. In comparison with lunar samples, the simulants exhibit similar poured bulk densities of 1.50g/cm^3 for EAC-1A, 1.60g/cm^3 for LMS-1 and 1.61g/cm^3 for LHS-1.

3.1.5 Thermal analysis

Regolith is a multi-constituent aggregate consisting of several mineralogical components. It is useful to understand the thermal behaviour of these components in order to estimate appropriate processing temperatures. A technique coupling Thermogravimetric Analysis (TGA) with Differential Scanning Calorimetry (DSC) was used to identify thermal transition temperatures for each sample. Using a calibrated Mettler Toledo TGA/DSC 3+ instrument, all three simulants were heated from room temperature to above 1400°C at a rate of 10K/min for EAC-1A and LHS-1 samples and a rate of 50K/min for LMS-1 sample. The tests were performed under an argon atmosphere with a constant gas flow of 70 ml/min. Additionally, a blank curve was obtained under the same conditions as each sample, in order to account for buoyancy and the effects of the instrument.

Figure 4 shows DSC curves normalized to sample temperature for EAC-1A, LMS-1 and LHS-1 simulants. All three samples exhibit transformations in the 1100 – 1350°C region. This is consistent with the melting of basalt, ilmenite and glass [86], [87] which are present in the given simulants in varying quantity, see Table 3. The exhibited thermal behaviour may also

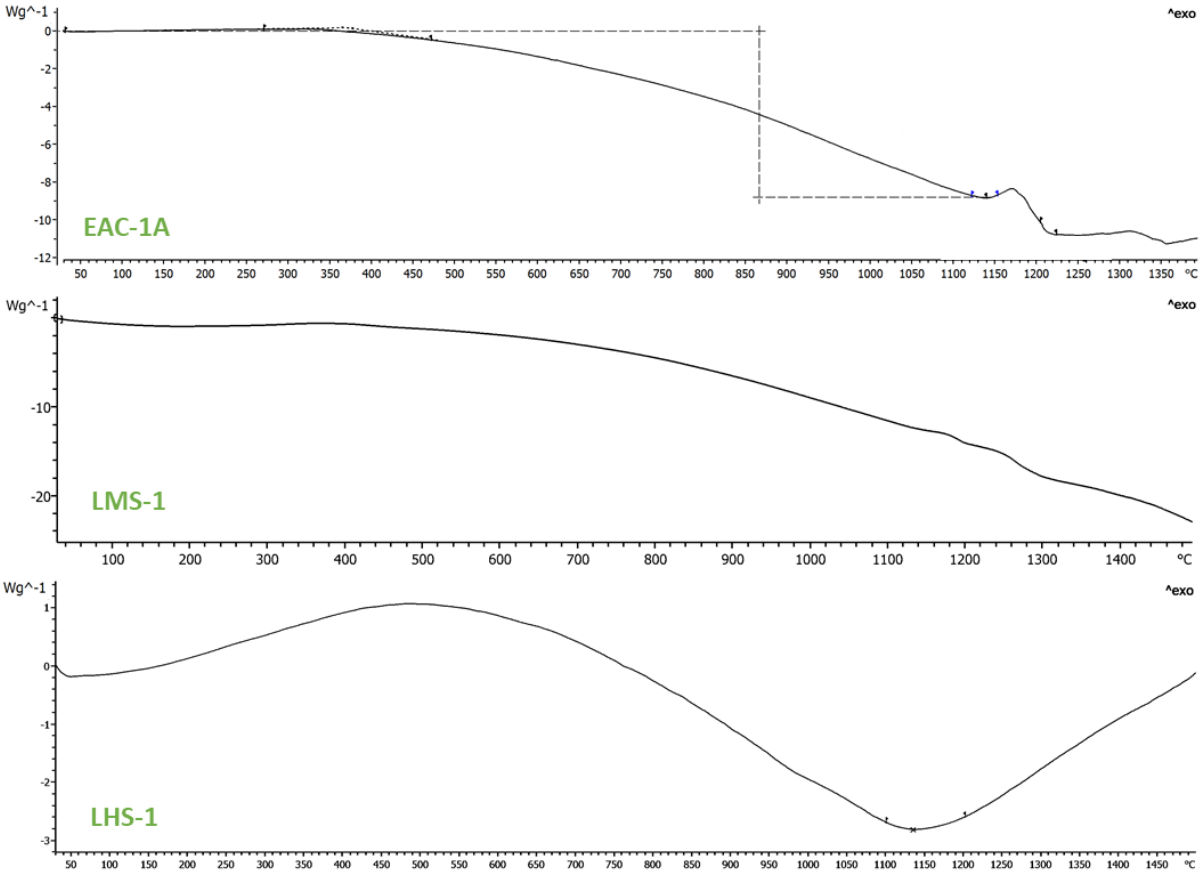

Figure 4. DSC traces for EAC-1A (above), LMS-1 (centre) and LHS-1 (below)

be attributed to the melting or partial-melting of plagioclase. In lunar regolith the plagioclase is assumed to be of the high-Ca type anorthite which has a melting temperature around 1550°C. However the presence of Na_2O oxide in the bulk chemistry suggests plagioclase may have undergone partial melting, as the plagioclase solidus temperature is known to decrease with increasing sodium content [88], [89]. Thus, at sintering temperatures in the range 1250 – 1350°C or above, some regolith melting should be expected.

From the TGA results, the following values of mass loss were recorded, in the temperature range 30 – 1350°C. When heated above 1350°C, mass losses of 0.97 % for LMS-1, 1.07 % for LHS-1 and 2.75 % for EAC-1A were observed. These losses can be attributed to loss of water and the release of other volatiles at higher temperatures. To emulate lunar surface conditions most effectively, simulants should be furnace dried to remove volatiles before processing.

3.2 Additive Manufacturing Consolidation Techniques

3.2.1 Digital Light Processing

Digital Light Processing (DLP) is a liquid-based additive manufacturing technique able to fabricate complex three-dimensional structures from ceramic or metallic powders. This vat polymerization method uses ultraviolet (UV) light to harden or cure a photopolymer resin, while a platform moves upward or downward after each new layer of the 3D printed object is cured [90][91]. DLP consists of three steps: 1) printing into required shape based on 3D model; 2) debinding to remove the polymeric binder; 3) sintering as a final step aimed at full consolidation.

In this study, DLP was performed using the EAC-1A powder. The original powder was sieved through a 30-μm sieve and the solid content of the slurry was set to 41%. Rectangular bars were 3D-printed with a layer thickness of 50 μm and a depth of cure of 100 μm. Water debinding was performed for 1 day followed by debinding in a furnace. Debinding in the furnace involved slow heating in air with stops at 150, 300, 400 and 600°C to obtain the optimal removal of the resin and to reduce the remaining carbon amount as much as possible. The bars were then sintered in a standard furnace in an air atmosphere. The first sintering temperature was set to 1050°C and kept for 1 hour, with a slow heating rate of 100°C/h. An additional sintering run at 1075°C was carried out to improve sintering of the bars.

Printing and debinding steps were successfully performed in the DLP process. However, the standard sintering step required further optimisation to obtain good densification. Spark Plasma Sintering was then introduced for optimisation of the sintering parameters.

3.2.2 Spark Plasma Sintering

Spark Plasma Sintering (SPS) is a manufacturing technique that utilizes uniaxial pressure and pulsed or unpulsed DC or AC current to consolidate powders into the required shape [92]. SPS has been previously studied as a technique to consolidate the lunar regolith simulants, metal powders, or functionally graded materials [93]–[97]. In this research, a Spark Plasma Sintering machine (SPS, FCT Group, Germany) operated under vacuum and a 20 mm graphite die with graphite punches was used. A 0.2 mm thick graphite foil was used to avoid adhesion and reaction between the powders and the graphite mould. Besides this foil, boron nitride spray was applied to reduce carbon diffusion into the sample. For this work, 4 mm high samples were pre-pressed to 10 kN before being set up into the SPS machine. The sintering parameters used for the different experiments of regolith are given in Table 4 while Table 5 shows the process parameters used for the consolidation of the metallic powders.

Table 4. Process parameters used for Spark Plasma Sintering of lunar regolith

No.	**Lunar regolith simulant**	**Sintering temperature (°C)**	**Pressure (MPa)**	**Holding time (min)**	**Maximum particle size (μm)**
1	LHS-1	900	80	10	200
2	LHS-1	975	80	20	100
3	LHS-1	975	80	20	50
4	LHS-1	1025	80	20	50
5	LHS-1	1050	80	20	50
6	LHS-1	1075	80	20	50
7	LMS-1	1050	80	20	50
8	EAC-1A	1050	80	20	22
9	EAC-1A	1050	80	20	50
10	EAC-1A	1050	80	20	100

Table 5. Process parameters used for Spark Plasma Sintering of metallic powder

Material	Sintering temperature (°C)	Pressure (MPa)	Holding time (min)	Maximum particle size (μm)
Stainless Steel 316L	1050	50	10	30
	1050	50	20	30
	1100	50	20	30
Ti_6Al_4V	1000	50	10	45
	1050	50	10	45

3.2.3 Laser Melting Additive Manufacturing

The lunar regolith simulant LMS-1 was used to perform some Laser Scanned lines using a Yb:YAG continuous disk laser with a wavelength of 1030 nm. The power was in the range of 160 – 8000 W and the scan speed was up to 200mm per second. The spot size at focus was 0.2 mm.

The powder was sieved through a 100 μm-sieve and deposited on a ceramic plate. In literature, some parameters were found to be optimized for selective laser melting or other laser additive manufacturing techniques of lunar regolith simulant. They had one common point which was a very low surface energy density, often less than 5 J/mm² [24], [98]–[100]The parameters had to be adapted to our own laser at TU Delft. The parameters used are shown below in Table 6 and were chosen to have the energy density as low as possible.

The base substrate was a ceramic plate commonly used for high temperature oven instead of the common steel substrate used with this laser because Sitta and Lavagna [100] observed poor wettability of the lunar regolith simulant on a steel substrate. Other metal substrates were used for their research, but they got the better results when using a refractory clay as a substrate.

Some trials on a steel plate have been performed to study the influence of substrate and determine the potential feasibility of using the lunar regolith as a coating on metallic substrate. The same parameters were kept for these trials. However, additional laser lines have been conducted: these lines were performed with an overlapping of 50 % to study the influence of remelting.

Table 6. Parameters for laser scanned lines.

Samples	Lunar regolith simulant	Maximum particle size (μm)	Laser Power (W)	Beam spot size (mm)	Scan speed (mm/s)
1	LMS-1	100	160	0,2	100
2				0,4	
3				0,6	

3.3 Microstructural and Morphological Characterisation

XRD analysis was performed to determine the phases in the original powders and in the consolidated samples. The analysis was performed with a Bruker D8 Advance diffractometer using Cu Kα radiation. The step size used was 0.033° 2θ with 45 kV and 40 mA current in a 2θ range of 10°-100°. The samples were ground with SiC 180 to remove the remaining graphite foil and to enable XRD analysis.

The density of the samples was measured based on Archimedes' principle. The samples were cleaned with isopropanol, dried and then weighed dry and immersed in distilled water.

Spark Plasma Sintered samples were discs of 20 mm diameter and 4 mm thickness. The specimens were cut into 2 half-discs, then embedded into a conductive resin, ground (SiC 80, 180, 320, 800, 1200 and 2000) and polished (MD Mol 3 µm and MD Nap 1 µm). Optical microscopy (Olympus BX60M) and Scanning Electron Microscopy (SEM) - in both secondary and backscattered modes - were used for microstructural characterization. Average porosity level and average relative sintered thickness were determined based on optical images. Energy Dispersive Spectroscopy (EDS) was performed to determine local composition and elemental distribution in the bulk and interface layers.

Thermocalc® calculations were performed to determine the phases formed at the interface of FGM based on EDS results.

Microhardness measurements were carried out using an automated Vickers hardness machine, Dura Scan (Struers). A load of 0.3 kgf (HV0.3) was used to measure the hardness of the lunar regolith sintered samples. It was observed that a higher load level results in severe cracking. For the metallic sintered samples, a load of 0.5 kgf (HV0.5) was used to measure their hardness. The hardness was measured at multiple locations on each sample and the average was calculated.

3.4 Finite Element Method: Simulation of DLP

The sintering stage can be modelled to be optimized or understood in the case of new materials. In order to model it, a continuum mechanics approach was chosen. Some models are done at microscopic levels to study the process at particles levels. In this study, a model at the macroscopic level was considered to evaluate shrinkage of the samples and temperature evolution within the sample [101].

The sample before sintering are porous medium and their behaviour can be studied by continuum mechanics. The solid is composed of a solid part (the particles) and porosities. The porosities are considered to be homogeneously distributed and the solid phase has an isotropic and non-linear viscous behaviour. During the sintering, it is expected that the porosity will decrease, and the density will increase: the sample shrinks during sintering. The relative density (ρ) is then related with the porosity (θ) level as follows:

$$\rho = 1 - \theta \quad (1)$$

During sintering, the sample shrinks and its volume decreases, but the mass remains the same. The mass conservation principle can be applied as follows:

$$\frac{\dot{\rho}}{\rho} = tr(\underline{\dot{\epsilon}}) \quad (2)$$

with $\underline{\dot{\epsilon}}$ the strain rate of solid phase.

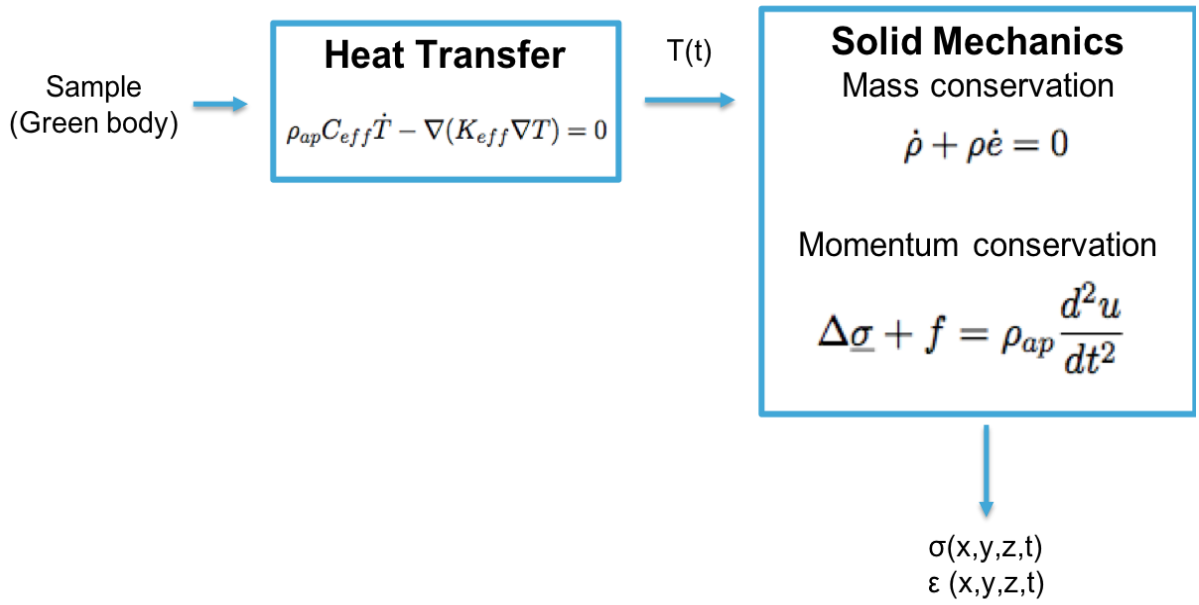

Figure 5. Schematic of simulation steps

Moreover, the momentum conservation law is applicable to continuum solid and the equation is as follow considering a quasi-static transformation:

$$\Delta\underline{\boldsymbol{\sigma}} + f = 0 \tag{3}$$

with $\underline{\sigma}$ the Cauchy stress tensor and f the external force applied.

The sintering process implies the heating of the powder and the mechanical phenomenon is coupled with a thermal phenomenon. The conservation energy equation is then:

$$\rho C_{eff}\dot{T} - \nabla\left(K_{eff}\nabla T\right) = \beta(\underline{\sigma}:\underline{\dot{\varepsilon}}_{vp} - \sigma_s\dot{e}) \tag{4}$$

with C_{eff} is the heat capacity, K_{eff} is the thermal conductivity, β is the viscoplastic work dissipated as heat (0 < β < 1), $\underline{\dot{\varepsilon}}_{vp}$ is the viscoplastic strain rate and finally $\dot{e}$ is the volumic strain rate.
In free sintering, stress and viscoplastic strain are negligible so the right side of the equation above equals 0. Both the heat capacity and the thermal conductivity depends on the temperature and the porosity level.

This continuum mechanics approach is summarized in the schematic in Figure 5

A viscoplastic constitutive model is applied to determine the deformation during sintering. Indeed, the deformation during sintering is controlled by diffusion and is comparable to creep induced deformation. Moreover, thermal expansion is also relevant in the case of sintering and must be added to the viscoplastic deformation. The deformation has then three main components: an elastic deformation, a thermal deformation and a viscoplastic deformation.

The strain rate is then:

$$\dot{\epsilon} = \dot{\epsilon_e} + \dot{\epsilon_{th}} + \dot{\epsilon_{vp}} \tag{5}$$

and the viscoplastic strain rate is divided as follows:

$$\dot{\epsilon_{vp}} = \dot{\epsilon_s} + \dot{\epsilon_c} \quad (6)$$

The elastic strain ϵ_e is determined by Hooke's law and the thermal strain ϵ_{th} depends on temperature and thermal expansion coefficient.

The viscoplastic strain is expressed as follows:

$$\dot{\epsilon_{vp}} = \frac{\underline{\sigma\prime}}{2G_p} + \frac{\sigma_m - \sigma_s}{3K_p}\underline{1} \quad (7)$$

with $\underline{\sigma'}$ the deviatoric stress, $\sigma_m = \frac{tr(\underline{\sigma})}{3}$ the hydrostatic stress and σ_s the sintering stress.

The parameters for the viscoplastic constitutive law can be determined by different models. The model chosen has been developed by Olevsky and Skorohod (SOVS model). It is a phenomenological model commonly used for the modelling of ceramic sintering. The parameters are then:

$$G_p = (1-\theta)^2\eta \quad (8)$$

$$K_p = \frac{4(1-\theta)^3\eta}{3\theta} \quad (9)$$

$$\sigma_s = \frac{3\gamma_{sv}(1-\theta)^2}{r_0} \quad (10)$$

with η the viscosity and γ_{sv} the surface energy.

This model has been implemented to Comsol Multiphysics®. The model consists of a heat transfer module and a solid mechanics module using the creep subroutine to implement the SOVS model.

4 Results and Discussion

4.1 Consolidation of Lunar Regolith

4.1.1 Digital Light Processing (DLP)

Figure 6 shows lunar regolith (EAC-1A) printed samples with a layer thickness of 50 μm. Four bars were successfully printed with a height and width of 5 mm and a length of 100 mm.

The debinding step was successful and the bars remained in its shape after being heat-treated. The colour of the samples after debinding was the same as the initial powder; hence no significant change of the composition of the powder should have occurred. It can thus be concluded that printing and debinding DLP steps can be performed without significant change in chemistry.

After standard (in air) sintering, the samples showed rather poor sintering characteristics: the bars did not keep their shape and cracked into small pieces. The sintered samples also changed in colour, to a light red. The similar colour change was also noticed by Liu et al. [102], who found it to be associated with the transformation of Fe^{2+} to Fe^{3+} via oxidation reactions.

Hence it can be concluded that standard in air sintering is not suitable for this material and further optimization of the sintering step is required.

The microstructure of the samples showed poor sintering between particles (see Figure 7). However, the structure also shows larger particles are surrounded by smaller particles, which would be beneficial for sintering as smaller particles can close the voids between coarser particles, thus resulting in better packing and densification. Furthermore, as shown in Figure 7b, some particles have coalesced and formed necking. Such observations as partial necking indicate that this material could be sintered with Digital Light Processing (DLP); however the sintering process requires further optimization, which is the scope of the follow up sections

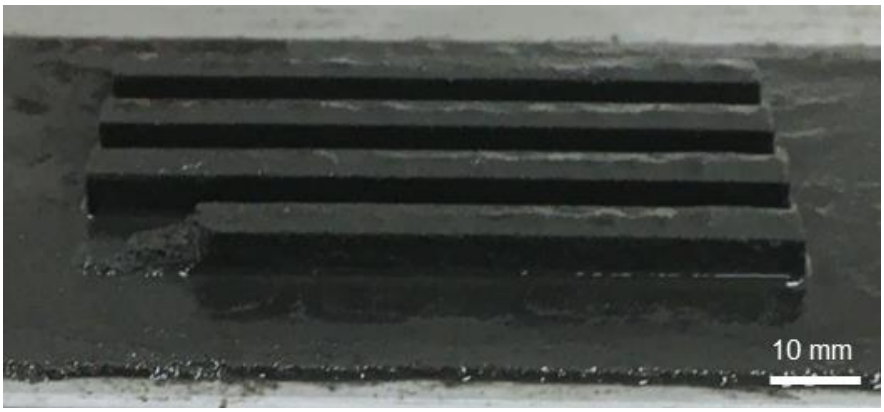

Figure 6. DLP printed bars made from lunar regolith simulant EAC-1A

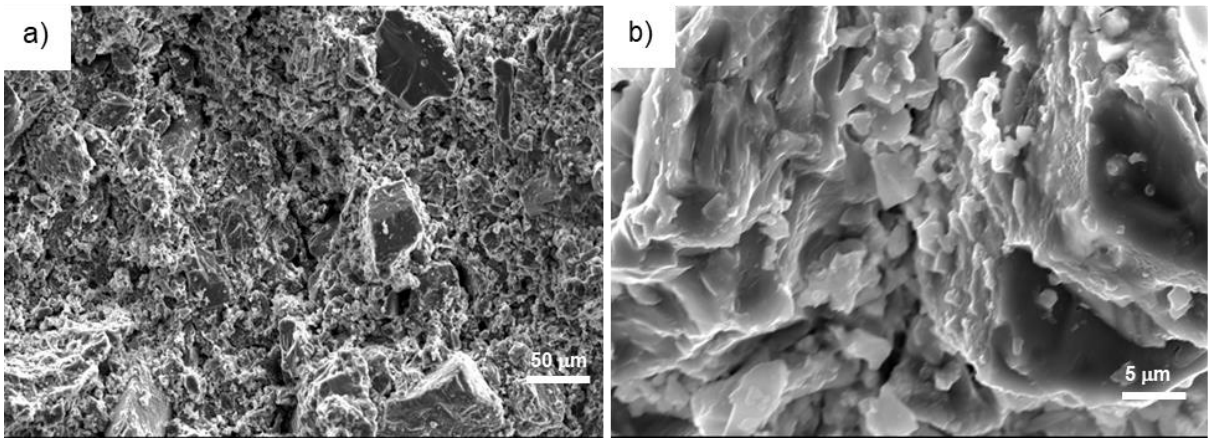

Figure 7. SEM images of DLP samples sintered under standard in air conditions: a) low magnification and b) high magnification).

4.1.2 Spark Plasma Sintering (SPS)

SPS is proposed as a follow-up to DLP to increase densification of the lunar regolith. A number of experiments were performed using SPS techniques to optimize the technique. The results were analysed with respect to the sintering temperature, initial powder particle size, and different compositions in the lunar regolith powders.

Effect of SPS temperature

Table 7 shows the effect of the SPS temperature on the density and hardness. As can be seen, SPS significantly increases the density and hardness while reducing the porosity of

lunar regolith simulant samples. The density was found to increase with the sintering temperature, with the maximum density of 2.704 ± 0.025 g.cm^{-3} achieved for the sample sintered at 1075°C. However, it should be noted, that sintering at 1075°C led to partial melting

Table 7. Density and Vickers hardness of SPS sintered lunar regolith (LHS-1) samples

SPS temperature (°C)	Density (g/cm^3)	Porosity (%)	Hardness $HV_{0.3}$
1025	2.532 ± 0.046	23.7 ± 5.4	443 ± 56
1050	2.616 ± 0.060	21.0 ± 5.5	725 ± 77
1075	2.704 ± 0.025	11.7 ± 3.3	743 ± 142

and resulted in a non-stable process. It is thus can be recommended to keep the sintering temperature below 1075°C.

The microstructure of the samples was studied with SEM/EDS and their phases were determined with XRD (Figure 8 and Figure 9). Three main phases were present in the samples at all sintering temperatures: an augite light grey phase [$Ca(Mg,Fe,Al)(Si,Al)_2O_6$], a sodian anorthite dark grey phase [$(Ca,Na)(Si,Al)_4O_8$] and a white phase corrresponding to an iron titanium oxide (Figure 8). During the SPS experiment, the sodian anorthite could have transformed to augite. The augite is often found in a form of “smashed” particles within the anorthite phase, as shown in Figure 9. This microstructure could be due to the pressure applied during SPS process. The partially dissolved anorthite can be pushed in between the smashed augite particles with the application of the external pressure. Anorthite has a lower melting point and a lower modulus than augite: anorthite is thus more prone to plastic deformation under the applied pressure and can fill the gaps between the smashed augite particles [103]. This specific microstructure was observed for all sintering temperatures.

The XRD patterns for the three different sintering temperatures were very similar: all samples exhibit the same diffraction peaks and are thus composed of the same minerals. This is in good accordance with the SEM images, since the same three phases are distinguished: augite, sodian anorthite and an iron titanium oxide. The compositions of the sintered samples are very similar to the composition of the as-received powder.

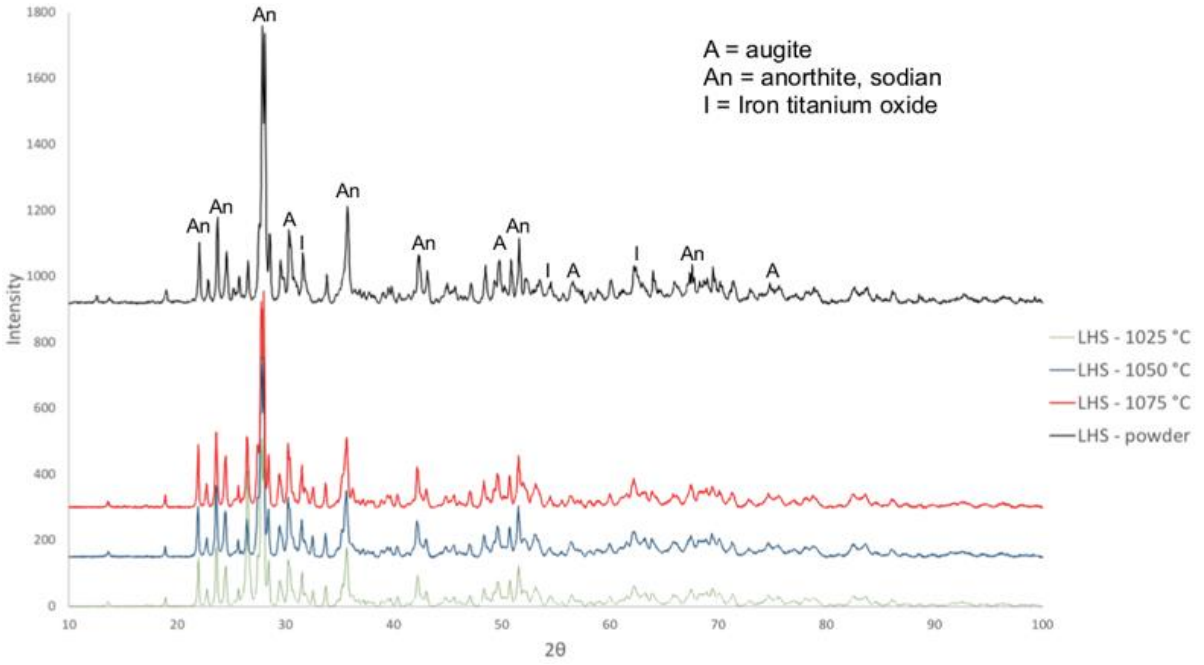

Figure 8. XRD patterns of LHS-1 sintered samples as compared to the LHS as-received powder

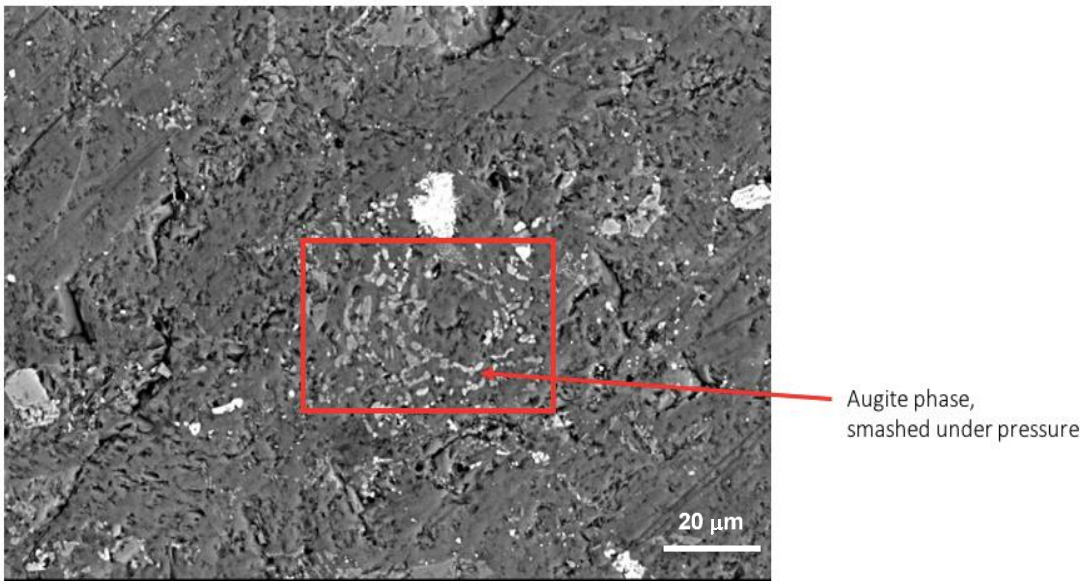

Figure 9. Microstructure of sintered LHS sample (at 1050 °C and 80 MPa)

Carbon was detected with EDS only on the outer part of the samples. This carbon originates from the graphite foil used to prevent the powder from sticking to the mould during SPS. Boron nitride was sprayed on the graphite foil to avoid this diffusion, but a small portion of carbon can still diffuse into the samples. Carbon diffusion is a thermally activated process: the carbon diffusion increases when using higher sintering temperatures and higher pressure. Carbon only penetrates over a small layer of the sample and this layer can be removed by mechanical polishing. On EDS, the carbon was homogeneously present and did not form any carbides.

The Vickers hardness was also found to increase with the temperature. A significant increase is observed between the sintering temperature of 1025°C and 1050°C. The hardness measurement is in accordance with the microstructure of the sintered samples. The high standard deviation is related to the different phases present in the specimens and the respective position of the measurement.

Effect of particle size

In order to evaluate the effect of particle size, EAC regolith samples with sieved powders of maximum particle size 22, 50, 100 µm were sintered at optimal temperature of 1050°C and 80 MPa.

As can be seen in Table 8. Density and Vickers hardness of SPS sintered lunar regolith (EAC) sample with different particle size. samples with smaller particle size show higher densification. Moreover, the standard deviation is higher for samples with coarser particles, which indicates that the microstructure is more heterogeneous. It should also be noted that more macro-pores were observed in the coarser 100 µm-sample. The presence of very coarse particles thus prevents good packing in the powder sample. The sample with the smallest initial particle size is the only sample that showed high densification along the vertical direction.

The higher densification of samples with finer powders can be related to several densification mechanisms: rearrangement of the particles, formation and growth of the sintering necks between the particles, and plastic deformation [104]. The smaller the particle size, the higher the surface energy driving force given in equation 1 is. This higher driving force, causing migration of particles and increasing the contact area between particles, enhances the sintering of powder.

Table 8. Density and Vickers hardness of SPS sintered lunar regolith (EAC) sample with different particle size.

Particle size (µm)	Density (g/cm^3)	Porosity (%)	Hardness $HV_{0.3}$
< 22	3.040 ± 0.046	4.3 ± 2.1	722 ± 35
< 50	2.831 ± 0.077	15.5 ± 6.2	752 ± 74
< 100	2.795 ± 0.078	21.4 ± 4.6	657 ± 46

$$\Delta E = E_p - E_d \approx \gamma_{sv} W_m S_p \quad (11)$$

$$S_p \propto \frac{1}{R} \quad (12)$$

Equation 1 and 2 show the relationship between powder properties and the driving force for sintering, with ΔE being the intrinsic driving force, E_p the surface energy of powder before sintering, E_d the surface energy of powder after sintering, γ_{sv} (J/m^2) the solid-gas surface energy, W_m (g/mol) the molar mass of material, S_p (cm^2/g) the specific surface area of powder and R the radius of the particle.

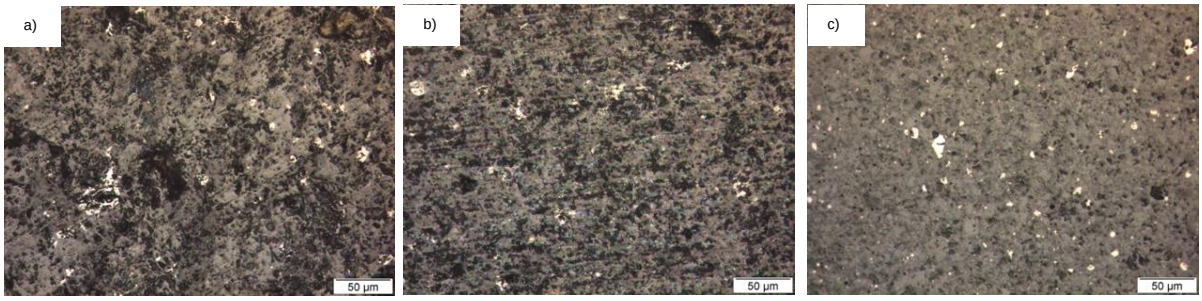

Figure 10. Optical microscopy images of EAC-1A sintered samples: a) 100 µm, b) 50 µm and c) 22 µm.

The tensile stress of the sintering necks increases with decreasing particles size and the strength of the sintering necks is higher between smaller particles. Only the use of crushed EAC-1A powder (with resulting 22 µm particles) led to a fully dense sample (Figure 10c). In the case of SPS, the particle surface is heated to high temperatures compared to the particle core due to spark discharge in the voids. In the case of small particles, the surface to volume ratio of the particle is bigger than for coarse particle. The amount of the powder subjected to high temperature is higher in the case of smaller particles, which leads to a more effective densification.

XRD patterns Figure 11) showed no significant differences between the samples consolidated with different particle sizes. The primary identified phases were plagioclase, pyroxenes (augite and diopside) and iron titanium oxide. The composition of the sintered samples is close to the composition of the initial powder.

The hardness of the sample with coarse particles is lower than for the other samples. The higher hardness for the sample with maximum particle size 50 µm is associated with a higher standard deviation due to the different hardness of the particles. The hardness of the 22 µm-sample and 50 µm-sample are thus comparable. The hardness does not increase with powder milling because the phase composition is the same; however, it is more homogeneously distributed.

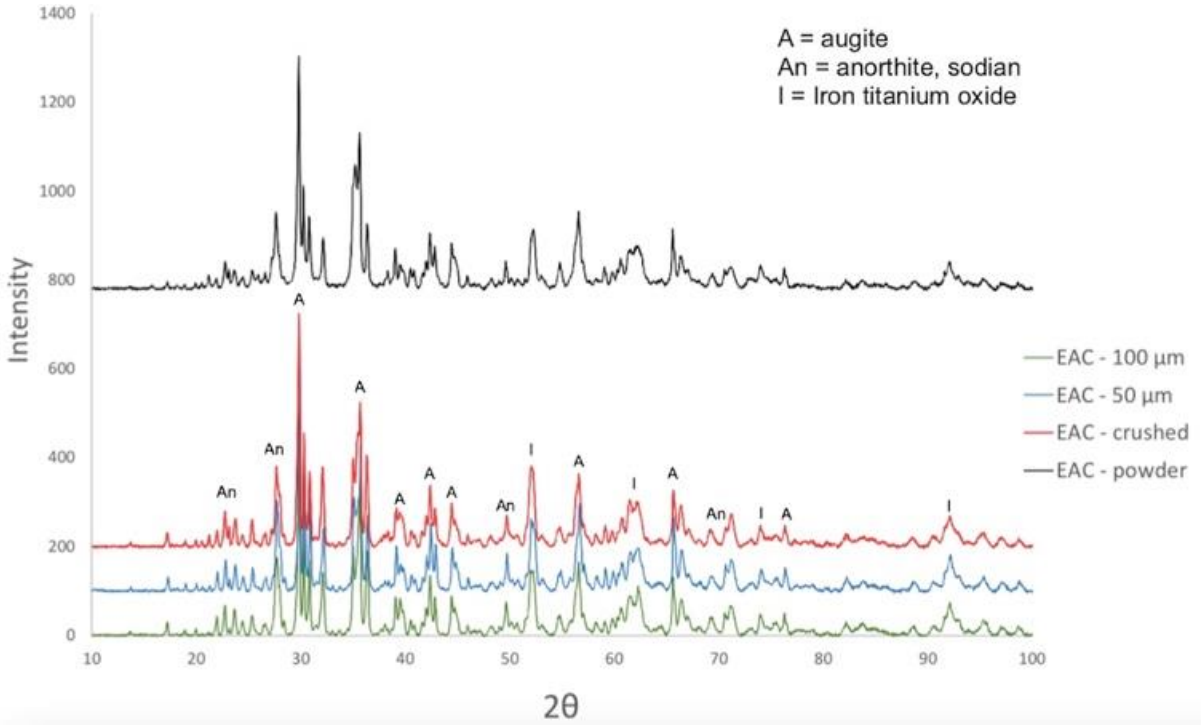

Figure 11. XRD patterns for SPS samples with different particle size as compared with as-received powder.

Effect of powder composition

In order to evaluate the effect of regolith simulants and their composition, the powders of LHS-1, EAC-1A and LMS-1 were Spark Plasma Sintered at the previously determined optimal conditions of 1050°C, 80 MPa pressure, maximum particle size of 50 µm with holding time of 20 min.

As can be seen from Table 9, all three simulants result in a similar densification level and none of the powders melted under these sintering conditions (1050°C, 80 MPa). EAC-1A and LMS-

1 samples showed higher densification than the LHS-1 samples. It should however be noted that a thicker layer of fully dense material was measured for the LHS-1 sample. This indicates that the average porosity is lower for LMS-1 and EAC-1A, but LHS-1 has a more heterogeneous porosity with a highly densified part. All three simulants were found to be composed of the same oxides and minerals: thus they have comparable temperature of phase transitions and a similar SPS behaviour can be expected.

The Vickers hardness of the samples was also unaffected by the difference in simulant's composition (Table 9). LMS has more iron titanium oxide phases and the standard deviation could be influenced by the presence of these phases at some locations of the material.

The microstructures of the sintered samples were also comparable and exhibited dense microstructures with three main phases: augite, sodian anorthite and iron titanium oxide. LMS-1 samples showed a higher content of iron titanium oxide and coarser particles of this oxide (white phases in Figure 12) than LHS-1 and EAC-1A samples.

4.2 Consolidation of Metallic Powders

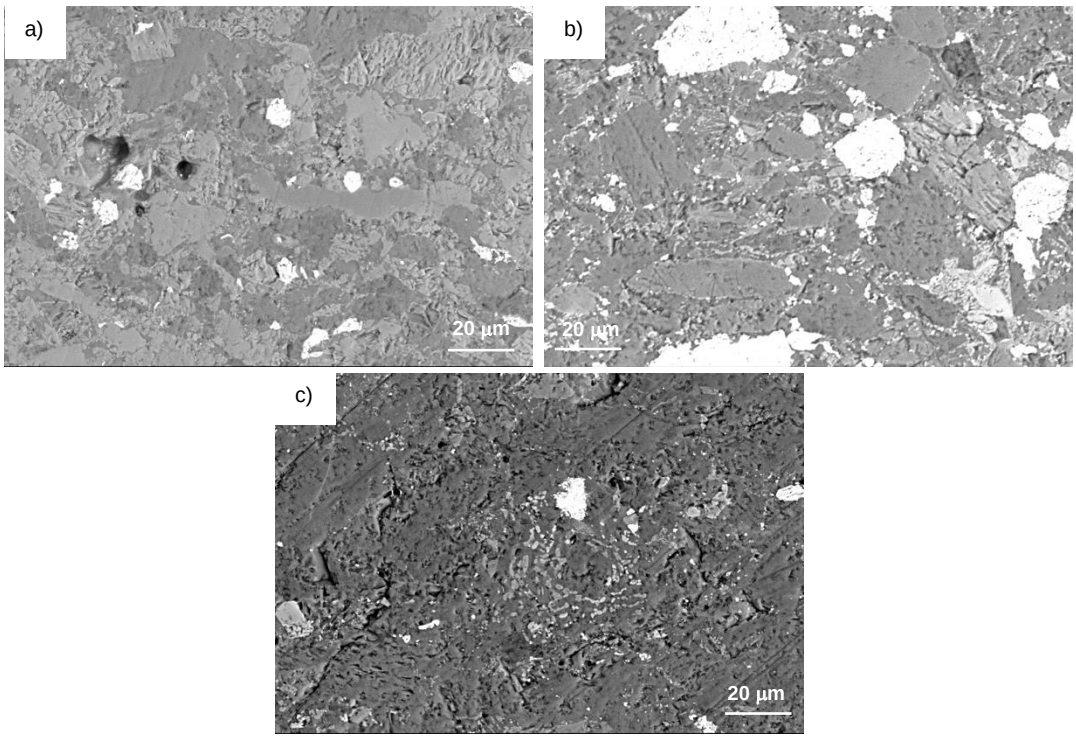

Figure 12. SEM images of SPS samples of three different lunar regolith simulants: a) EAC-1A, b) LMS-1 and c) LHS-1

In order to develop a functionally graded material featuring the combination of lunar regolith and metallic alloys, consolidation of both individual materials should first be understood and optimised. In previous sections, consolidation of lunar regolith and influencing parameters were discussed. In this section SPS consolidation of stainless steel and Ti_6Al_4V will be addressed.

Table 8 shows optimization of SPS parameters based on density and hardness. As can be seen, increasing the sintering temperature increases the density and hardness of stainless steel. The observed density decrease is relatively low with increased holding time; other authors observed the opposite trend [105]. The lower density in this case could be due to poor rearrangement of the particles during sintering, preventing the pores from closing, or could be due to a different balance between open pores and closed pores, as the Archimedes measurements only take into account the open pores. However, when porosity is measured using optical techniques, the porosity reduces with increasing temperature.

All Ti_6Al_4V samples showed good densification and almost zero porosity. The applied uniaxial pressure of 50 MPa helps to rearrange the particles, breaking the agglomerates and inducing

Table 9. Density and Vickers hardness of SLS samples of different regolith simulants (max particle size 50 µm).

Lunar regolith simulant type	Density (g/cm^3)	Porosity (%)	Hardness $HV_{0.3}$
LHS-1	2.616 ± 0.060	21.0 ± 5.5	725 ± 77
EAC-1A	2.831 ± 0.077	15.5 ± 6.2	752 ± 74
LMS-1	2.817 ± 0.083	21.6 ± 7.7	732 ± 167

plastic deformation at high temperatures. Moreover, another mechanism of densification is important: the Joule heating effect derived from the pulsed current. The current can flow through the highly conductive powdered sample, heating up the particles, especially at particle surfaces. The temperature is thus higher at the contact point between particles; the diffusion increases and leads to a higher and easier densification [106].

The hardness (Table 10) for both alloys was found to increase with increasing sintering temperature. The hardness for the samples sintered at 1050°C is in the order of the hardness of cast annealed 316 alloys. The samples sintered at 1100°C show a much higher hardness. The hardness was homogeneous across the whole sample and the standard deviation is relatively small for all samples, indicating that the microstructure and composition are also likely homogeneous. SEM analysis revealed a homogeneous microstructure for all samples and did not show any precipitates. Some nano precipitates could be present, such as carbides due to carbon diffusion, however they are not visible under the magnification used. Some authors reported the presence of carbides on grain boundaries [105], however these carbides were only found on the samples' thin edges.

The Vickers hardness for Ti_6Al_4V was found to be 341 $HV_{0.5}$ for the samples sintered at 1050°C compared to 322 $HV_{0.5}$ for the sample sintered at 1000 °C. These values are in the order of the Vickers hardness for Ti_6Al_4V cast alloys [107].

XRD results shown in Figure 13 reveal only austenite phase present in all 316L samples. This fully austenitic microstructure was also observed by Keller et al. [108].

For Ti_6Al_4V alloys, the elements Ti, Al and V were found to be evenly distributed, and no precipitates were formed during the sintering process. XRD results (Figure 14) showed that the same phases forms at the two different sintering temperatures. The α-Ti phase is present as in the as-received powder, but a second phase is detected for both samples: $Ti_{0.8}V_{0.2}$ which is a β-Ti structure.

Microstructural analysis revealed the presence of clusters of grains elongated in the same direction. Recrystallization is not hindered by the presence of intermetallics at the grain boundaries or by interstitial solute atoms, as shown by Long et al. [96].

Table 10. Density and Vickers hardness of sintered stainless steel and Ti6Al4V (under 50MPa pressure)

Material	Temperature / Holding time	Density (g/cm^3)	Porosity (%)	Hardness $HV_{0.5}$
Stainless steel 316	1050 °C/10 min	7.642 ± 0.046	3 ± 1.2	158 ± 5
	1050 °C/20 min	7.556 ± 0.015	1.4 ± 0.4	164 ± 6
	1100 °C/20 min	7.834 ± 0.010	0.9 ± 0.3	191 ± 5
Ti_6Al_4V	1000 °C/10 min	4.391 ± 0.018	1.2 ± 0.5	322 ± 11
	1050 °C/10 min	4.389 ± 0.006	0.7 ± 0.2	341 ± 23

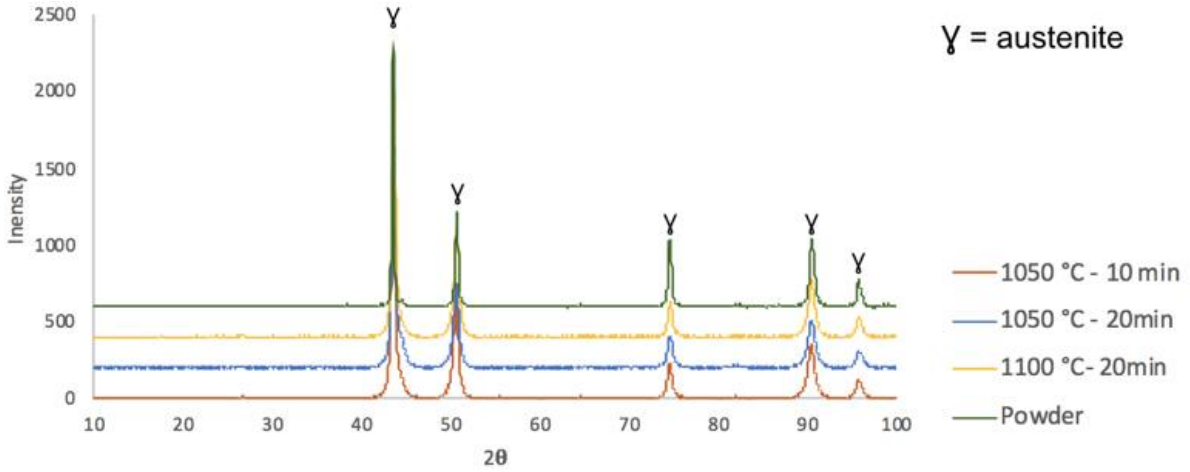

Figure 13. XRD of SPSed stainless steel 316 samples and of as-received powder

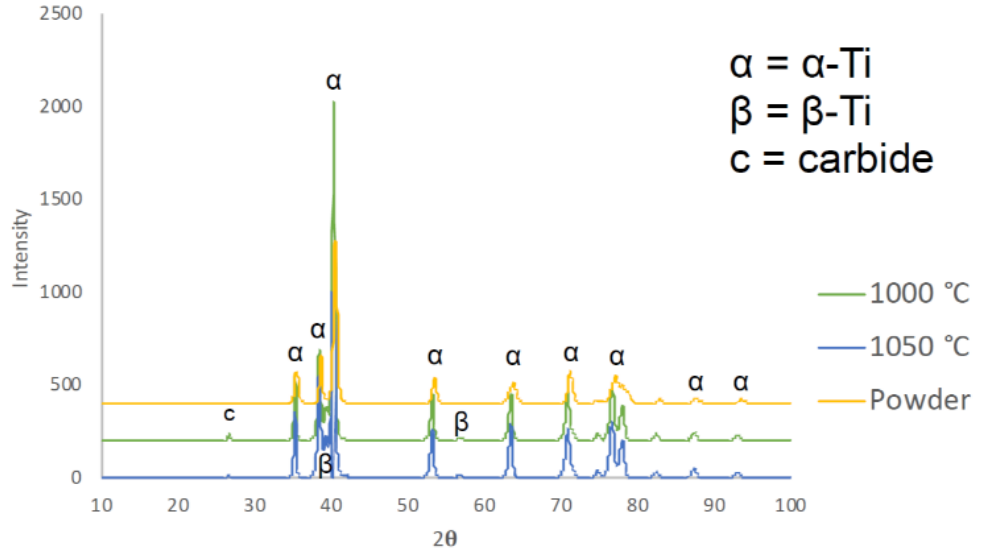

Figure 14. XRD patterns of sintered Ti6Al4V and as-received powder.

4.3 Consolidation of Functionally Graded Material

The optimized parameters for FGM samples were based on sintering results from regolith simulant and individual metallic powders. The optimal SPS parameters for each material are given in Table 11.

Table 11. Optimal SPS parameters of FGM based on lunar regolith simulant, stainless steel and titanium alloy.

Material	Sintering temperature (°C)	Pressure (MPa)	Holding time (min)	Maximum particle size (mm)
Lunar regolith simulant EAC-1A	1050	80	20	22
Stainless steel 316L	1100	50	20	30
Ti_6Al_4V	1050	50	10	45

4.3.1 FGM Composite of Regolith and Stainless Steel (316L)

The sintering experiments combining both lunar regolith (EAC-1A) and 316L were first performed in one SPS step, which resulted in an inconsistent FGM and interfacial cracking. The one-step sintering at 1100°C under 50 MPa completely melted the lunar regolith simulant, which was squeezed out of the SPS mould. The surface of the metallic part did not show any remnants of the lunar regolith. This experiment highlights that sintering at 1100°C under 50 MPa is not suitable for the FGM lunar regolith simulant.

When sintering both powders at 1050°C under 50 MPa, the FGM did not keep its shape and EAC-1A and stainless steel layers did not bond. Both layers exhibited cracks and porosity at the FGM interface (Figure 15).Thus pressure of 50 MPa proved too low to allow good sintering of the two powders: a minimal pressure of 80 MPa seemed to be required to sinter the lunar regolith and a high pressure may also be required to allow interfacial sintering.

Two-step sintering was then introduced and proven to be more successful; a thin layer of EAC-1A remained in contact with the metal. However, the FGM fractured within the lunar regolith layer upon removal from the SPS mould. The coefficient of thermal expansion of stainless steel 316 is twice higher than that of lunar regolith [109]. This mismatch in thermal properties induces thermal stresses during SPS cooling and these stresses can explain why the FGMs cracked post-sintering. The interface between the two dissimilar materials, however, remained intact. SEM images revealed the presence of a grey phase at the interface, featuring higher chromium concentration than in the inner layers (Figure 16a). Chromium tends to diffuse to the interface from the stainless steel and form a high-content Cr phase; according to Thermocalc® calculations and composition from EDS, this is likely to be a BCC-A2 phase (Figure 16c).

The hardness profile (Figure 17) for the 316L/EAC functionally graded material showed that the interface has much closer hardness to the metallic alloy and does not exhibit a gradual transition, which is preferred for FGMs. Since the change in hardness between the interface and the lunar regolith is relatively large, it could explain the poor sintering properties of this type of FGM.

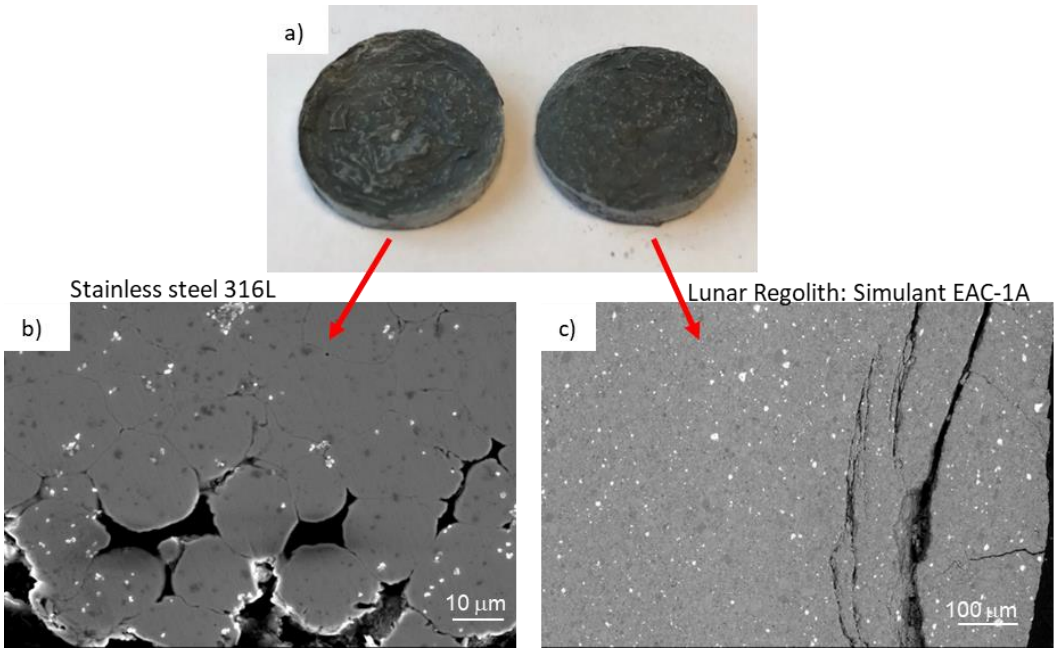

Figure 15. a) FGM 316/EAC after sintering at 1050°C. SEM images of the interface between the two materials: b) SS 316L and c) EAC-1A.

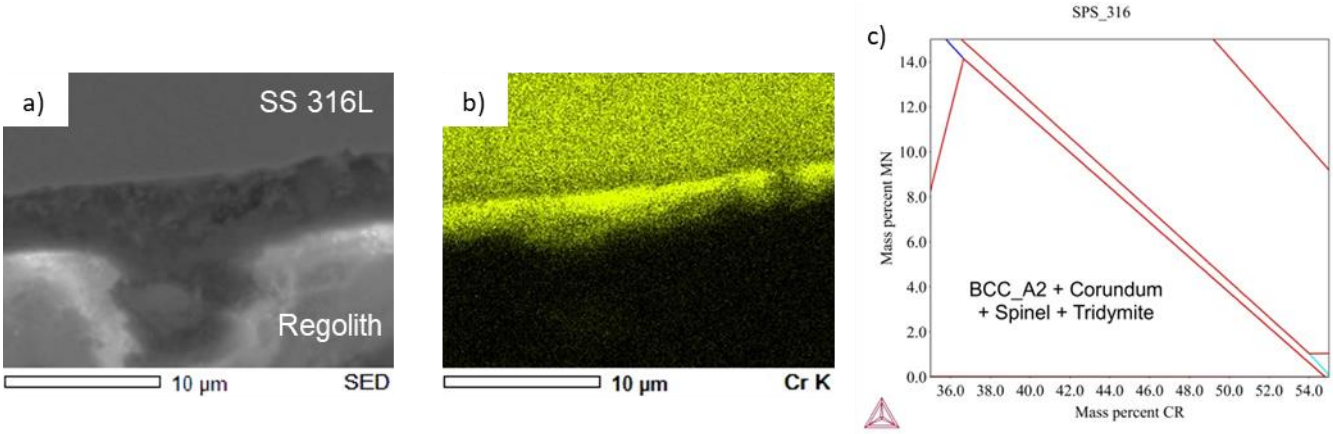

Figure 17. a) SEM image of interface of FGM 316/EAC, b) EDS map of Cr at the interface of FGM 316/EAC and c) Thermocalc graph for Cr diffusion.

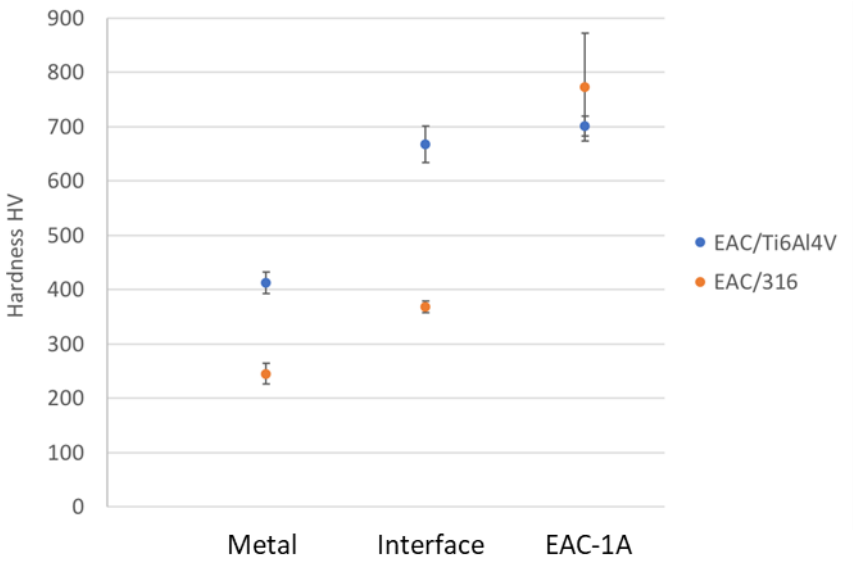

Figure 16. Vickers hardness profile of the functionally graded materials.

4.3.2 FGM Composite of Regolith and Ti_6Al_4V Alloy

The second type of alloy chosen in this work for its good compatibility with lunar regolith was Ti_6Al_4V. The produced FGM samples (Figure 18) did not show any fracture, cracking or interfacial porosity characteristic to the previous 316L/EAC FGM. As shown in Figure 18b, white particles, identified as titanium oxide, are present at the interface between the lunar regolith and Ti_6Al_4V. Moreover, EDS measurements reveal a potential segregation of silicon at the interface (Figure 19b) which forms the phase HCP_A3 (Ti_xSi_y) according to Thermocalc® calculations (Figure 19c)

The Vickers hardness profile of this FGM shows a gradual transition at interface from one material to another (Figure 17). The hardness of the interface is close to the hardness of the lunar regolith. The coefficient of thermal expansion of Ti_6Al_4V and lunar regolith simulant are very close (about $8x10^{-6}$ K^{-1} for both materials [109]–[111]), which helps to avoid high thermal stresses during sintering and especially during the cooling stage.

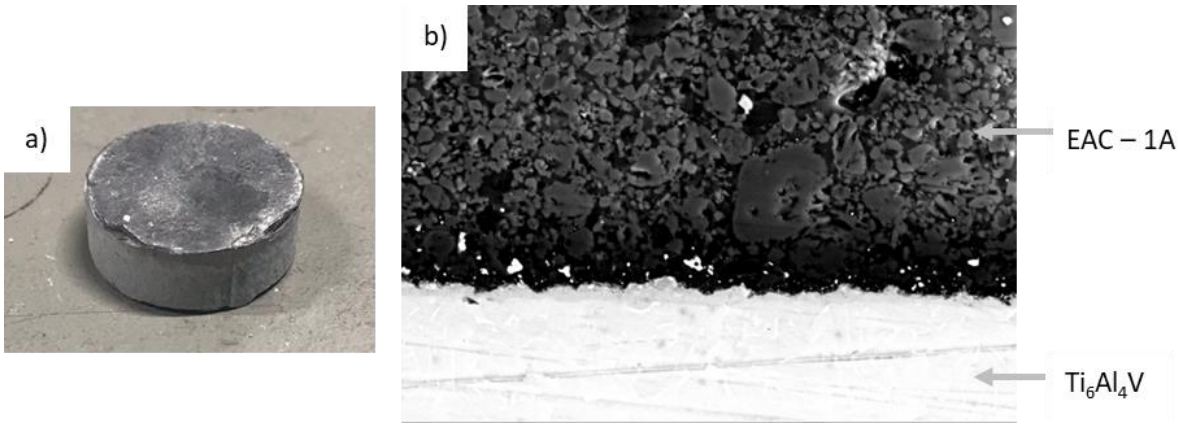

Figure 18. a) FGM Ti6Al4V/EAC-1A after sintering in 2 steps and b) SEM image of the interface between Ti_6Al_4V and EAC-1A

4.4 Laser Scanning

During the Spark Plasma Sintering runs, some melting of the lunar regolith simulant powders happened when higher temperatures were tried. The EAC-1A powder melted during the one-step SPS run for the FGM samples with stainless steel at 1100 °C and a trial at 1200 °C was also made to see the effect of pressure on the DLP powder. Melting of the powder at temperature around 1100 °C was a starting point for the trial of laser additive manufacturing technique. The lunar regolith could be used as a cladding for metallic parts to protect them against environment issues. A laser based additive manufacturing technique could eventually be used to manufacture whole FGM.

Three different spot size have been chosen for the laser lines trials that give three different energy densities. The first observation with naked eye is that higher spot size (i.e. smaller energy density) results in a more continuous line. Indeed, when using higher energy density, only a portion of the powder melts and sticks to the ceramic plate as on Figure 20. However, even the smaller energy density gives an incomplete laser line: smaller energy might be required, or the inhomogeneous surface of the used plate could also be a reason for incomplete melted lines.

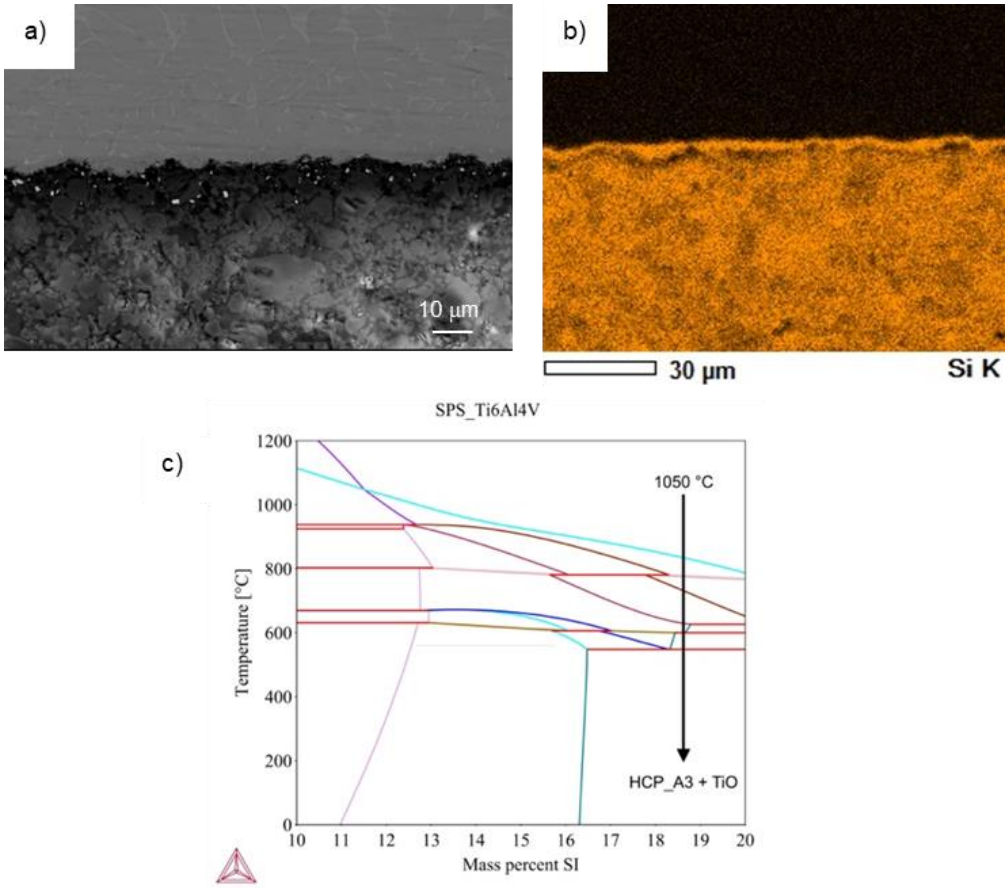

Figure 20. a) SEM image of interface of FGM Ti_6Al_4V/EAC, b) EDS of Si at the interface of FGM and Ti_6Al_4V c)Thermocalc graph for Ti_6Al_4V/EAC interface.

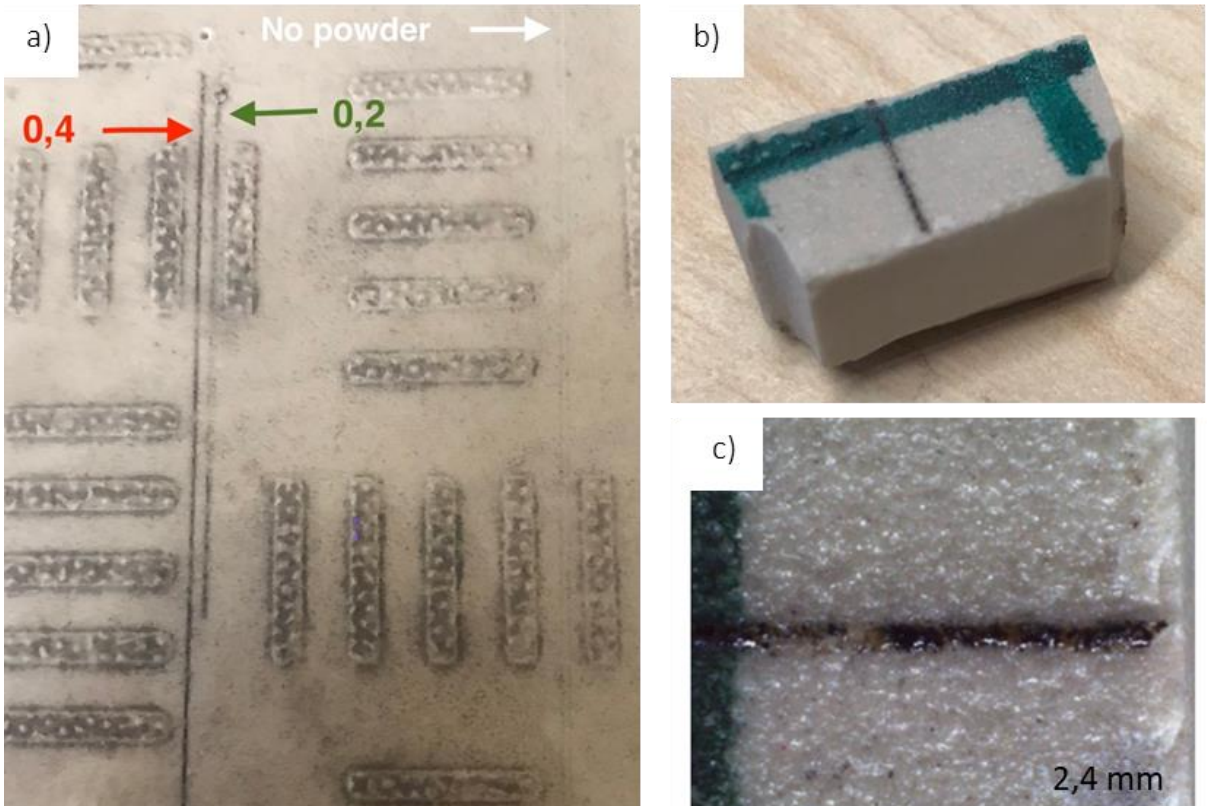

Figure 19. Laser scanned lines: a) 2 laser scanned lines with different laser spot size and 1 line without powder, b) & c) laser scanned lines with laser spot size of 0,6 mm

The morphologies of the laser lines are relatively similar. The tracks exhibit the microstructure of solidified layer after being molten. The surface is smooth and exhibits patterns of a melt pool such as some “waves”. Besides, they all exhibit cracks perpendicular to the scanning direction of the laser. These cracks could result from thermal stresses arisen during the cooling of the liquid powder or due to thermal stresses between the plate and the solidified regolith powder.

Only a small portion of particles are seen on the SEM images indicating that the powder almost completely melted during the laser melting experiments: the energy density is then enough to melt the powder. However, the particles of the lunar regolith have different composition and the softening/melting point differs between minerals. The parameters for technique like selective laser melting should then be optimized to melt all different minerals without causing too much defects.

The big holes on the SEM image on Figure 23 might be related to a default in the powder bed: a lack of powder could explain this. Moreover, on SEM images, some small holes are present. The lunar regolith simulants have particles with irregular shapes and they cannot be smoothly spread on the substrate as spherical particles can be. These irregularities create inconsistent voids in the powder which lead to inhomogeneous mass distribution and so inhomogeneous energy intensity. The melt pool is thus inconsistent, and voids can be created due to irregularities in the powder shape.

Some trials were made on a steel substrate. The powder was successfully melted and stuck partially to the substrate when one line was made. On Figure 22 the laser lines appear incomplete for two reasons, either because the melted powder did not stick during laser melting or because the laser-melted powder came off while removing the extra powder after the laser melting experiments. The sticking of the melted powder proved to be poor. Moreover, some lines were made with an overlap of 50 % to obtain a wider area. During the second run, the laser-melted lines came off the substrate.

The XRD analysis of the scanned lines did not show many peaks indicating crystalline phases. The material turned amorphous during laser melting. The peaks seen on XRD pattern (Figure 21) correspond to main phase of the powder: sodian anorthite. The laser trials can be related to the SPS experiments. Indeed, the poor sticking of the powder to the steel plate is in accordance with the trials of FGM with stainless steel and lunar regolith simulant.

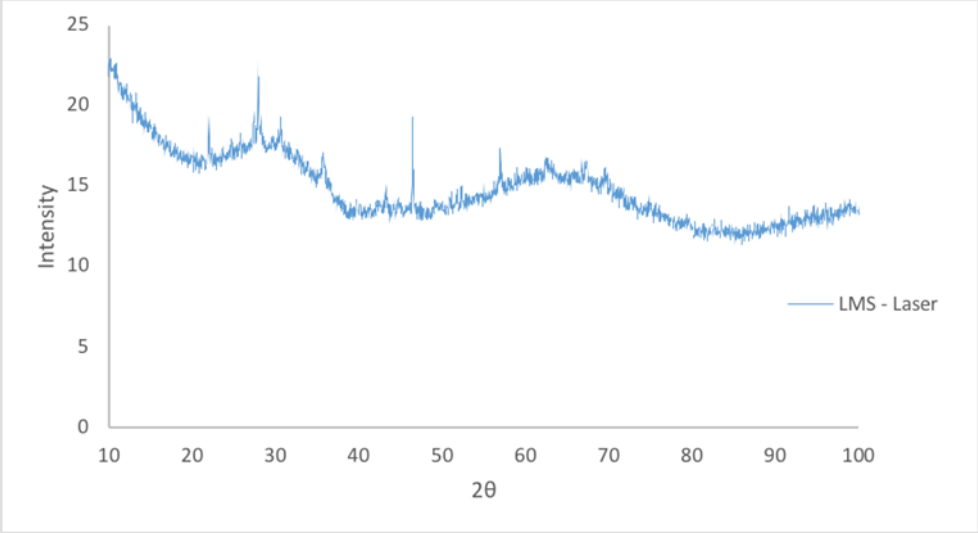

Figure 21. XRD of laser sintered lines

Figure 23. Laser lines on steel plate

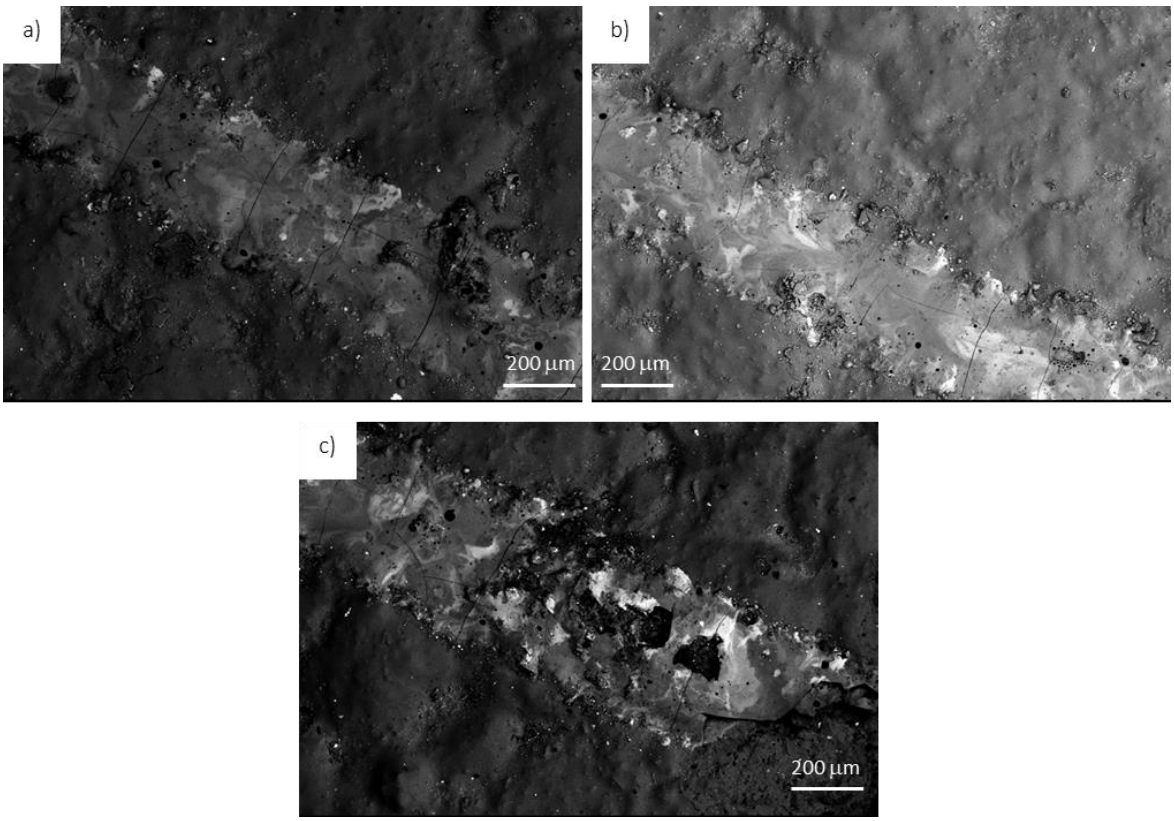

Figure 22. SEM images of laser melted lunar regolith simulant LMS-1 with different spot size: a) 02mm, b) 0.4mm amd c) 0.6mm

4.5 Finite Element Method: Simulation of DLP

A simulation has been developed to study the sintering of the powder when applying only temperature, as in the case of the sintering stage in Digital Light Processing. The thermal and viscous properties of the slurry used in DLP required for the model are unknown so properties from literature have been used. The simulation is thus to be improved with proper properties. However, this model can be used to evaluate the stresses within the samples and the temperature gradient during sintering.

Different tests have been performed to evaluate the effect of heating rate, temperature and average particle size. The results are summed up in the tables below. The temperature gradient corresponds to the difference of temperature between the surface and the centre at the end of the heating. The porosity gradient is defined as the difference of porosity between the centre and the side of the samples. The samples are discs of a diameter of 20 mm and an initial height of 5 mm.

Table 12. Influence of the heating rate on sintering

Heating rate (°C/min)	Maximum stress (N/m^2)	ΔT (°C)	Porosity gradient
2	$2{,}2.10^{-4}$	0,5	-
10	$2{,}36.10^{-4}$	3	-
50	$2.8.10^{-4}$	5	-
100	1.10^{-5}	33	-

Table 13. Influence of the sintering temperature on sintering

Sintering temperature (°C)	Maximum stress (N/m^2)	ΔT (°C)	Porosity gradient
1050	$1{,}25.10^{-4}$	1	-
1100	$1{,}53.10^{-4}$	0,6	-
1150	$2{,}2.10^{-4}$	0,5	-
1200	$3{,}02.10^{-4}$	0,5	-

Table 14. Influence of average particle size on sintering.

Average particle size (μm)	Maximum stress (N/m^2)	ΔT (°C)	Porosity gradient
1	$2{,}2.10^{-4}$	0,5	-
5	$4{,}4.10^{-5}$	0,5	-
10	$2{,}52.10^{-5}$	0,5	-
50	$6{,}6.10^{-6}$	0,6	-

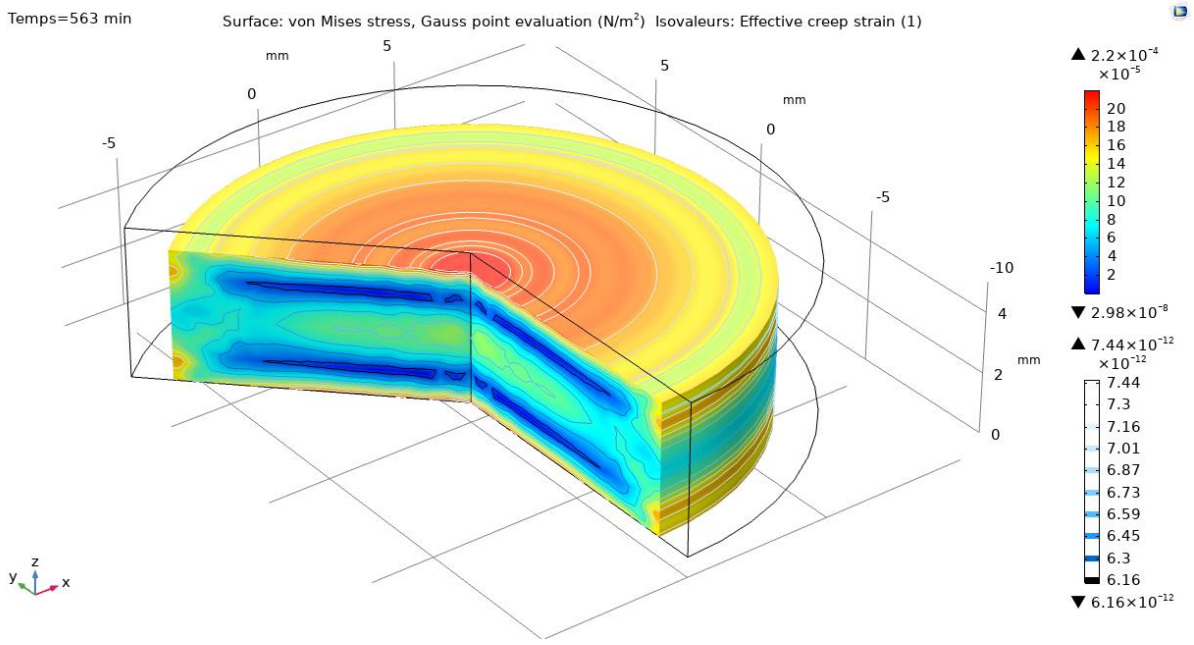

Figure 25. 3D stresses after sintering at 1150 °C, with an average particle size of 1 µm and a heating rate of 2°C/min

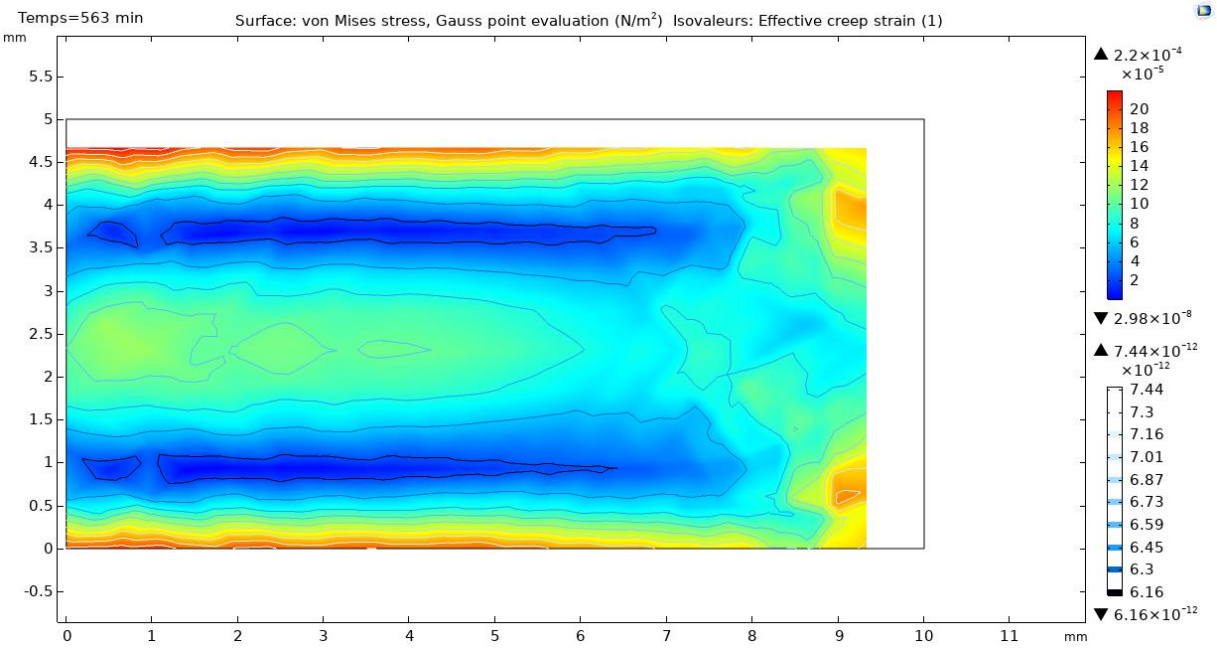

Figure 24. 2D stresses after sintering at 1150 °C, with an average particle size of 1 µm and a heating rate of 2 °C/min

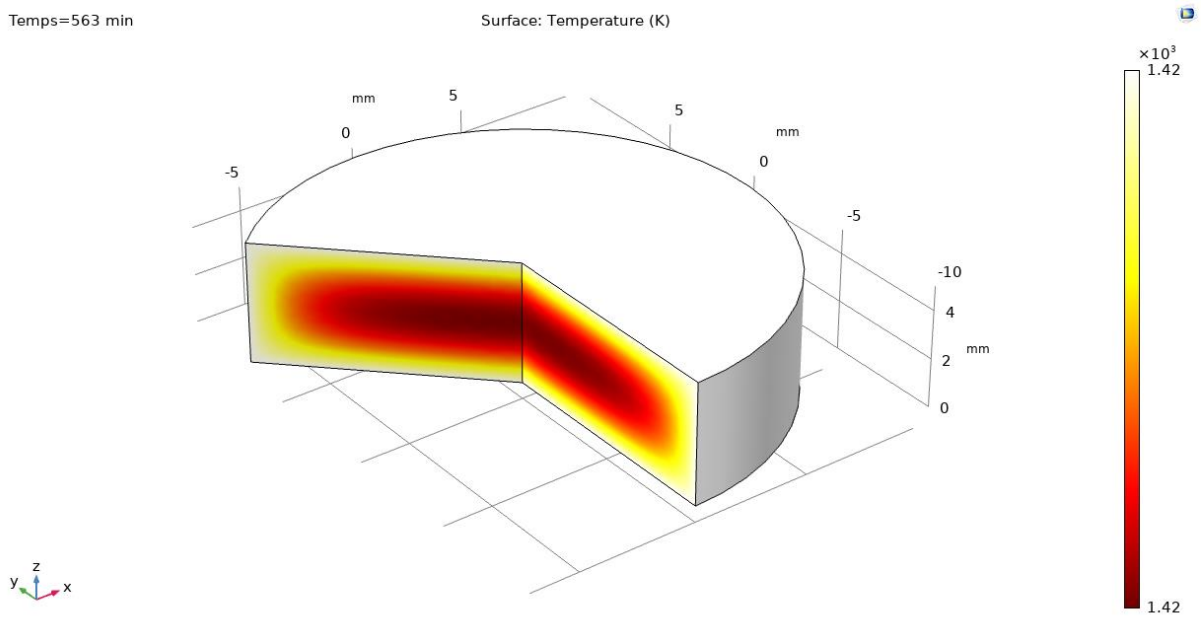

Figure 26. Temperature profile in sintered sample.

In the study of the heating rate (Table 12) an initial porosity of 47%, an average particle size of 1 μm and a sintering temperature of 1150 °C are fixed for all the different simulations. It can be seen that using a high heating rate cause a high gradient of temperature. This high gradient of temperatures can cause stresses within the sample and inhomogeneity in the sintering process. The porosity gradient is not relevant for any heating rate even if the temperatures are not homogeneous. It could be related to the temperature of 1150 °C which is high enough to provide good sintering.

The stresses are higher on the edges and especially on the top and bottom surface. It is related to the higher temperatures and to the gradient of temperature. Indeed, a higher temperature enables higher consolidating of the particles and higher deformation. (Figure 24 - Figure 26)

In the table below, the influence of the sintering temperature is shown. The same particle size of 1 μm and a heating of 2 °C/min were fixed. Higher sintering temperature gives higher stresses and so higher deformation. However, temperature higher than 1200 °C causes too high non-linearity of the model which could be an evidence of potential local melting of the powder. Using a low heating rate for these simulations can explain the very low temperature gradient.

The influence of the average particle size is given in Table 14. A sintering temperature of 1150 °C and a heating rate of 2 °C/min were fixed for these simulations. The coarser the particles, the poorest the sintering is. The stresses and strains decrease significantly when using high average particle size. It relates to the poor sintering obtained during the DLP experiments done with the lunar regolith simulant.

5 Conclusions

In situ resource utilization is crucial for future space habitation on the Moon. In this study, additive manufacturing consolidation techniques of lunar regolith simulants have been examined and optimized in order to study the functional grading feasibility with metallic substrates. For this purpose, first lunar regolith simulants were printed and debinded using Digital Light Processing. Then Spark Plasma Sintering, using different sintering conditions (temperature, particle size and composition), was applied and optimized. The same SPS approach was applied towards metallic powders. Finally, the optimal processing conditions for consolidation of functionally graded regolith were developed with respect to densification, microstructural, compositional and microhardness characteristics. In parallel to the FGM experiments, laser scanning method was used to investigate the influence of laser melting on regolith consolidation, as well as the interfacial properties between the melted regolith and the substrate. Furthermore, a simulation of sintering characteristics of regolith was carried out using the Finite Element Method (FEM), to evaluate the post-sintering stresses in sintered DLP samples and the influences of processing parameters on these stresses.

The following conclusions are drawn from this study:

1. Three regolith simulants were characterised and found to be comparable to Apollo regolith samples in their composition, particle size distribution and density. All simulants exhibited a significant large grain (>1mm) fraction. Thermal analysis revealed a transformation attributed to partial melting occuring in the 1100 – 1350°C temperature range for all simulants.

2. Lunar regolith simulants can be successfully additively manufactured with combination of Digital Light Processing and Spark Plasma Sintering at 1050°C under 80 MPa. For best densification it is required to sieve or mill the powders to 20–50 µm range. A higher pressure could be used to avoid the milling step. Both increasing the temperature and reducing the particle size were found to increase densification and Vickers micro-hardness.

3. Metallic powders can be fully densified with SPS at relatively low temperature and a pressure of 50 MPa. Both stainless steel and Ti_6Al_4V showed homogeneous structure without precipitates or carbides.

4. FGMs were made using the optimal SPS parameters. The combination of lunar regolith and Ti_6Al_4V was shown as the most promising. The hardness profile showed a gradual transition between the two layers and the interface was found strong enough to avoid cracking.

5. The lunar regolith simulants melt at low enough temperature to allow laser-based manufacturing. A low energy is required to melt the powder and make it stick to the substrate. The bonding of the lunar regolith to a steel plate is poor whereas the bonding to a ceramic substrate is very strong.

6. Simulation with FEM model reveals that sample stresses are highest at the edges and especially the top and bottom surfaces. Higher heating rates lead to lower maximum stress and thus lower shrinkage and densification of the powder. Moreover, high heating rates result in an increased temperature gradient between the sample centre and surface, which results in higher thermal stresses and inhomogeneity.

5.1 Future Work

This feasibility study of FGMs using additive manufacturing and in-space resources showed promising results. However, further investigations on the mechanical properties of regolith-metallic FGMs, as well as combination of regolith with other metals such as aluminium, should be performed.

The DLP process performed well in constructing complex shapes, however the sintering step requires optimisation. The use of milled ultra-fine powders (less than 5 μm) could be investigated to ascertain the feasibility of sintering in a non-pressurised environment.

SPS technique would have to be modified to be employed on the Moon for large scale production, and the fidelity of large scale samples in terms of residual stresses and porosity homogeneity should be investigated in order to scale-up the process.

Laser scanning also showed promise as a method for manufacturing regolith coatings, but further work is required to improve interfacial properties with metallic substrates to avoid delamination.

The simplified FEM model would be improved by studying the thermal properties of sintered specimens and implementing these results into the simulation

6 Acknowledgements

The researchers would like to express gratitude to the ESA technicians at ESTEC and ECSAT for their support of this project, in particular to Advenit Makaya, Sarah Rodríguez Castillo, and Martina Meisnar.

We would also like to thank Jaap Hooijmans at Admatec for assisting with the DLP processing.

Lastly we would like to thank Jia Fu and Jia-Ning Zhu at TU Delft for their support with SPS experiments and Thermocalc calculations.

7 References

[1] H. Benaroya, *Building Habitats on the Moon: Engineering Approaches to Lunar Settlements*. Springer, 2018.

[2] P. Eckart, *Lunar base handbook*. McGraw-Hill Primis Custom Pub., 1999.

[3] A. S. Howe and B. Sherwood, *Out of this world: The new field of space architecture*. American Institute of Aeronautics and Astronautics, 2009.

[4] M. Z. Naser and A. I. Chehab, 'Materials and design concepts for space-resilient structures', *Prog. Aerosp. Sci.*, vol. 98, pp. 74–90, 2018.

[5] J. Frank, L. Spirkovska, R. McCann, L. Wang, K. Pohlkamp, and L. Morin, 'Autonomous mission operations', in *2013 IEEE Aerospace Conference*, Mar. 2013, pp. 1–20, doi: 10.1109/AERO.2013.6496927.

[6] K. Kennedy, 'The vernacular of space architecture', in *AIAA Space Architecture Symposium*, 2002, p. 6102.

[7] G. B. Sanders *et al.*, 'Results from the NASA capability roadmap team for in-situ resource utilization (ISRU)', 2005.

[8] J. J. Papike, S. B. Simon, and J. C. Laul, 'The lunar regolith: Chemistry, mineralogy, and petrology', *Rev. Geophys.*, vol. 20, no. 4, Art. no. 4, 1982.

[9] J. Edmunson and D. L. Rickman, 'A Survey of Geologic Resources', in *Moon*, Springer, 2012, pp. 1–21.

[10] T. H. Prettyman *et al.*, 'Elemental composition of the lunar surface: Analysis of gamma ray spectroscopy data from Lunar Prospector', *J. Geophys. Res. Planets*, vol. 111, no. E12, Art. no. E12, 2006.

[11] S. R. Taylor, 'The unique lunar composition and its bearing on the origin of the Moon', *Geochim. Cosmochim. Acta*, vol. 51, no. 5, Art. no. 5, 1987.

[12] C. M. Pieters, 'Composition of the lunar highland crust from near-infrared spectroscopy', *Rev. Geophys.*, vol. 24, no. 3, Art. no. 3, 1986.

[13] S. Mueller, G. J. Taylor, and R. J. Phillips, 'Lunar composition: A geophysical and petrological synthesis', *J. Geophys. Res. Solid Earth*, vol. 93, no. B6, Art. no. B6, 1988.

[14] W. AGOSTO, 'BENEFICIATION AND POWDER METALLURGICAL PROCESSING OF LUNAR SOIL METAL', in *4th Space manufacturing; Proceedings of the Fifth Conference*, American Institute of Aeronautics and Astronautics, 2020.

[15] G. A. Landis, 'Materials refining on the Moon', *Acta Astronaut.*, vol. 60, no. 10–11, Art. no. 10–11, 2007.

[16] C. C. Allen, R. V. Morris, and D. S. McKay, 'Oxygen extraction from lunar soils and pyroclastic glass', *J. Geophys. Res. Planets*, vol. 101, no. E11, Art. no. E11, 1996, doi: 10.1029/96JE02726.

[17] N. Labeaga-Martínez, M. Sanjurjo-Rivo, J. Díaz-Álvarez, and J. Martínez-Frías, 'Additive manufacturing for a Moon village', *Procedia Manuf.*, vol. 13, pp. 794–801, 2017.

[18] B. Khoshnevis *et al.*, 'Lunar contour crafting-a novel technique for ISRU-based habitat development', in *43rd AIAA Aerospace Sciences Meeting and Exhibit*, 2005, p. 538.

[19] M. Fateri *et al.*, 'Solar Sintering for Lunar Additive Manufacturing', *J. Aerosp. Eng.*, vol. 32, no. 6, Art. no. 6, 2019.

[20] M. Fateri, S. Pitikaris, and M. Sperl, 'Investigation on wetting and melting behavior of lunar regolith simulant for additive manufacturing application', *Microgravity Sci. Technol.*, vol. 31, no. 2, Art. no. 2, 2019.

[21] ‘Mechanical behaviour of additively manufactured lunar regolith simulant components - Athanasios Goulas, Jon GP Binner, Daniel S Engstrøm, Russell A Harris, Ross J Friel, 2019’, Nov. 01, 2020. https://journals.sagepub.com/doi/full/10.1177/1464420718777932?casa_token=fH2p9ug-ecoAAAAA%3AMKi2NKTDhxKRWxQRN_A65t4ebWqIntUr7WFbGaqbQqYgV22ab8dilHDvuSS1HLR7jJr3u65XcOWG (accessed Nov. 01, 2020).
[22] G. Cesaretti, E. Dini, X. De Kestelier, V. Colla, and L. Pambaguian, ‘Building components for an outpost on the Lunar soil by means of a novel 3D printing technology’, *Acta Astronaut.*, vol. 93, pp. 430–450, Jan. 2014, doi: 10.1016/j.actaastro.2013.07.034.
[23] A. Goulas, J. G. P. Binner, R. A. Harris, and R. J. Friel, ‘Assessing extraterrestrial regolith material simulants for in-situ resource utilisation based 3D printing’, *Appl. Mater. Today*, vol. 6, pp. 54–61, Mar. 2017, doi: 10.1016/j.apmt.2016.11.004.
[24] A. Goulas and R. J. Friel, ‘3D printing with moondust’, *Rapid Prototyp. J.*, vol. 22, no. 6, Art. no. 6, Jan. 2016, doi: 10.1108/RPJ-02-2015-0022.
[25] A. Meurisse, J. C. Beltzung, M. Kolbe, A. Cowley, and M. Sperl, ‘Influence of Mineral Composition on Sintering Lunar Regolith’, *J. Aerosp. Eng.*, vol. 30, no. 4, Art. no. 4, Jul. 2017, doi: 10.1061/(ASCE)AS.1943-5525.0000721.
[26] J. M. Neves, S. Ramanathan, P. Suraneni, R. Grugel, and A. Radlińska, ‘Characterization, mechanical properties, and microstructural development of lunar regolith simulant-portland cement blended mixtures’, *Constr. Build. Mater.*, vol. 258, p. 120315, Oct. 2020, doi: 10.1016/j.conbuildmat.2020.120315.
[27] D. Vaniman, R. Reedy, G. Heiken, G. Olhoeft, and W. Mendell, ‘The lunar environment’, *Lunar Sourceb. CUP*, pp. 27–60, 1991.
[28] M. B. Bever and P. E. Duwez, ‘Gradients in composite materials’, *Mater. Sci. Eng.*, vol. 10, pp. 1–8, 1972.
[29] A. Kawasaki and R. Watanabe, ‘Concept and P/M fabrication of functionally gradient materials’, *Ceram. Int.*, vol. 23, no. 1, pp. 73–83, 1997, doi: 10.1016/0272-8842(95)00143-3.
[30] D. Mahmoud and M. Elbestawi, ‘Lattice Structures and Functionally Graded Materials Applications in Additive Manufacturing of Orthopedic Implants: A Review’, *J. Manuf. Mater. Process.*, vol. 1, no. 2, p. 13, 2017, doi: 10.3390/jmmp1020013.
[31] M. Srivastava, S. Rathee, S. Maheshwari, and T. K. Kundra, ‘Design and processing of functionally graded material: review and current status of research’, in *3D Printing and additive manufacturing technologies*, Springer, 2019, pp. 243–255.
[32] Y. li Gao, C. shan Wang, M. Yao, and H. bin Liu, ‘The resistance to wear and corrosion of laser-cladding Al2O3ceramic coating on Mg alloy’, *Appl. Surf. Sci.*, vol. 253, no. 12, pp. 5306–5311, 2007, doi: 10.1016/j.apsusc.2006.12.001.
[33] X. Zhang, Y. Chen, and J. Hu, ‘Recent advances in the development of aerospace materials’, *Prog. Aerosp. Sci.*, vol. 97, pp. 22–34, 2018.
[34] X. Wang *et al.*, ‘Thermal protection system integrating graded insulation materials and multilayer ceramic matrix composite cellular sandwich panels’, *Compos. Struct.*, vol. 209, pp. 523–534, 2019, doi: 10.1016/j.compstruct.2018.11.004.
[35] M. Srivastava, S. Rathee, S. Maheshwari, and T. K. Kundra, ‘Design and processing of functionally graded material: review and current status of

research', in *3D Printing and additive manufacturing technologies*, Springer, 2019, pp. 243–255.
[36] B.-H. Kim and Y.-H. Na, 'Fabrication of fiber-reinforced porous ceramics of Al2O3-mullite and SiC-mullite systems', *Ceram. Int.*, vol. 21, no. 6, Art. no. 6, 1995.
[37] S. Suresh and A. Mortensen, 'Functionally graded metals and metal-ceramic composites: Part 2 Thermomechanical behaviour', *Int. Mater. Rev.*, vol. 42, no. 3, Art. no. 3, 1997.
[38] X. Zhang, Y. Chen, and J. Hu, 'Recent advances in the development of aerospace materials', *Prog. Aerosp. Sci.*, vol. 97, pp. 22–34, 2018.
[39] V. A. Popovich, E. V. Borisov, V. Heurtebise, T. Riemslag, A. A. Popovich, and V. S. Sufiiarov, 'Creep and thermomechanical fatigue of functionally graded Inconel 718 produced by additive manufacturing', in *TMS annual meeting & exhibition*, 2018, pp. 85–97.
[40] V. K. Balla, P. P. Bandyopadhyay, S. Bose, and A. Bandyopadhyay, 'Compositionally graded yttria-stabilized zirconia coating on stainless steel using laser engineered net shaping (LENS^{TM})', *Scr. Mater.*, vol. 57, no. 9, Art. no. 9, 2007.
[41] F. Gong, J. Zhao, Z. Li, J. Sun, X. Ni, and G. Hou, 'Design, fabrication and mechanical properties of multidimensional graded ceramic tool materials', *Ceram. Int.*, vol. 44, no. 3, Art. no. 3, 2018.
[42] Q. Jin, X. P. Ren, H. L. Hou, Y. L. Zhang, and H. T. Qu, 'In Situ Synthesis and Structural Design of Ti/TiC Functionally Graded Materials', in *Materials Science Forum*, 2018, vol. 913, pp. 515–521.
[43] F. F. Kamaruzaman, D. M. Nuruzzaman, N. M. Ismail, Z. Hamedon, A. Iqbal, and A. Azhari, 'Microstructure and properties of aluminium-aluminium oxide graded composite materials', in *IOP Conference Series: Materials Science and Engineering*, 2018, vol. 319, pp. 1–6.
[44] A. Katz-Demyanetz, V. V. Popov Jr, A. Kovalevsky, D. Safranchik, and A. Koptioug, 'Powder-bed additive manufacturing for aerospace application: Techniques, metallic and metal/ceramic composite materials and trends', *Manuf. Rev.*, vol. 6, 2019.
[45] S. W. Maseko, A. P. I. Popoola, and O. S. I. Fayomi, 'Characterization of ceramic reinforced titanium matrix composites fabricated by spark plasma sintering for anti-ballistic applications', *Def. Technol.*, vol. 14, no. 5, Art. no. 5, 2018.
[46] T. A. G. Restivo *et al.*, 'Micrograded ceramic-metal composites', *J. Eur. Ceram. Soc.*, vol. 39, no. 12, Art. no. 12, 2019.
[47] T. P. D. Rajan and B. C. Pai, 'Developments in processing of functionally gradient metals and metal–ceramic composites: a review', *Acta Metall. Sin. Engl. Lett.*, vol. 27, no. 5, Art. no. 5, 2014.
[48] A. J. Ruys, E. B. Popov, D. Sun, J. J. Russell, and C. C. J. Murray, 'Functionally graded electrical/thermal ceramic systems', *J. Eur. Ceram. Soc.*, vol. 21, no. 10–11, Art. no. 10–11, 2001.
[49] G. H. Heiken, D. T. Vaniman, and B. M. French, 'Lunar sourcebook-A user's guide to the moon', *Res. Support. NASA Camb. Engl. Camb. Univ. Press 1991 753 P No Individ. Items Are Abstr. This Vol.*, 1991.
[50] M. F. McKay, D. S. McKay, and M. B. Duke, 'Space resources. Volume 2: Energy, power, and transport', 1992.

[51] B. A. Lomax, M. Conti, N. Khan, N. S. Bennett, A. Y. Ganin, and M. D. Symes, ‘Proving the viability of an electrochemical process for the simultaneous extraction of oxygen and production of metal alloys from lunar regolith’, *Planet. Space Sci.*, p. 104748, 2019.
[52] M. Ivosevic, R. Knight, S. R. Kalidindi, G. R. Palmese, and J. K. Sutter, ‘Solid particle erosion resistance of thermally sprayed functionally graded coatings for polymer matrix composites’, *Surf. Coat. Technol.*, vol. 200, no. 16–17, pp. 5145–5151, 2006, doi: 10.1016/j.surfcoat.2005.05.038.
[53] G. E. Knoppers, J. W. Gunnink, J. Van Den Hout, and W. P. Van Vliet, ‘The reality of functionally graded material products’, *Proc. Solid Free. Fabr. Symp.*, pp. 38–43, 2004.
[54] Q. Shu-heng, Y. Jun-li, C. Xue-min, Z. Lin, and L. Le-ping, ‘Preparation of phosphoric acid-based porous geopolymers’, *Appl. Clay Sci.*, vol. 50, no. 4, pp. 600–603, 2010, doi: 10.1016/j.clay.2010.10.004.
[55] H. A. Toutanji, S. Evans, and R. N. Grugel, ‘Performance of lunar sulfur concrete in lunar environments’, *Constr. Build. Mater.*, vol. 29, pp. 444–448, 2012, doi: 10.1016/j.conbuildmat.2011.10.041.
[56] C. Buchner, R. H. Pawelke, T. Schlauf, A. Reissner, and A. Makaya, ‘A new planetary structure fabrication process using phosphoric acid’, *Acta Astronaut.*, vol. 143, no. October 2017, pp. 272–284, 2018, doi: 10.1016/j.actaastro.2017.11.045.
[57] R. Dou *et al.*, ‘Sintering of lunar regolith structures fabricated via digital light processing’, *Ceram. Int.*, vol. 45, no. 14, pp. 17210–17215, 2019, doi: 10.1016/j.ceramint.2019.05.276.
[58] X. Zhang *et al.*, ‘Microstructure evolution during spark plasma sintering of FJS-1 lunar soil simulant’, *J. Am. Ceram. Soc.*, no. September, pp. 1–13, 2019, doi: 10.1111/jace.16808.
[59] A. Meurisse, A. Makaya, C. Willsch, and M. Sperl, ‘Solar 3D printing of lunar regolith’, *Acta Astronaut.*, vol. 152, pp. 800–810, 2018.
[60] S. Maleksaeedi, H. Eng, F. E. Wiria, T. M. H. Ha, and Z. He, ‘Property enhancement of 3D-printed alumina ceramics using vacuum infiltration’, *J. Mater. Process. Technol.*, vol. 214, no. 7, pp. 1301–1306, 2014, doi: 10.1016/j.jmatprotec.2014.01.019.
[61] S. Rana and R. Fangueiro, *16 - Conclusions and future trends*. Elsevier Ltd, 2016.
[62] Y. Hu and W. Cong, ‘A review on laser deposition-additive manufacturing of ceramics and ceramic reinforced metal matrix composites’, *Ceram. Int.*, vol. 44, no. 17, pp. 20599–20612, 2018, doi: 10.1016/j.ceramint.2018.08.083.
[63] D. C. Hofmann *et al.*, ‘Developing gradient metal alloys through radial deposition additive manufacturing’, *Sci. Rep.*, vol. 4, 2014, doi: 10.1038/srep05357.
[64] Y. Zhang and A. Bandyopadhyay, ‘Direct fabrication of compositionally graded Ti-Al2O3multi-material structures using Laser Engineered Net Shaping’, *Addit. Manuf.*, vol. 21, pp. 104–111, 2018, doi: 10.1016/j.addma.2018.03.001.
[65] R. N. Grugel and H. Toutanji, ‘Sulfur “concrete” for lunar applications - Sublimation concerns’, *Adv. Space Res.*, vol. 41, no. 1, pp. 103–112, 2008, doi: 10.1016/j.asr.2007.08.018.
[66] M. Fateri and A. Gebhardt, ‘Process parameters development of selective Laser Melting of lunar regolith for on-site manufacturing applications’, *Int. J. Appl. Ceram. Technol.*, vol. 12, no. 1, pp. 46–52, 2015, doi: 10.1111/ijac.12326.

[67] A. Goulas, R. A. Harris, and R. J. Friel, ‘Additive manufacturing of physical assets by using ceramic multicomponent extra-terrestrial materials’, *Addit. Manuf.*, vol. 10, pp. 36–42, 2016, doi: 10.1016/j.addma.2016.02.002.
[68] C. J. Bae, A. Ramachandran, K. Chung, and S. Park, ‘Ceramic stereolithography: Additive manufacturing for 3D complex ceramic structures’, *J. Korean Ceram. Soc.*, vol. 54, no. 6, pp. 470–477, 2017, doi: 10.4191/kcers.2017.54.6.12.
[69] ‘SLA vs. DLP: Guide to Resin 3D Printers’, *Formlabs*. https://formlabs.com/eu/blog/resin-3d-printer-comparison-sla-vs-dlp/ (accessed Dec. 08, 2020).
[70] M. Liu *et al.*, ‘Digital light processing of lunar regolith structures with high mechanical properties’, *Ceram. Int.*, vol. 45, no. 5, Art. no. 5, Apr. 2019, doi: 10.1016/j.ceramint.2018.12.049.
[71] P. Cavaliere, Ed., *Spark Plasma Sintering of Materials: Advances in Processing and Applications*. Springer International Publishing, 2019.
[72] L. Song *et al.*, ‘Vacuum sintered lunar regolith simulant: Pore-forming and thermal conductivity’, *Ceram. Int.*, vol. 45, no. 3, pp. 3627–3633, 2019, doi: 10.1016/j.ceramint.2018.11.023.
[73] E. J. Faierson, K. V. Logan, B. K. Stewart, and M. P. Hunt, ‘Demonstration of concept for fabrication of lunar physical assets utilizing lunar regolith simulant and a geothermite reaction’, *Acta Astronaut.*, vol. 67, no. 1–2, pp. 38–45, 2010, doi: 10.1016/j.actaastro.2009.12.006.
[74] M. A. Hobosyan and K. S. Martirosyan, ‘Sintering of Regolith by Activated Thermites: A Novel Approach for Lunar In-Situ Resource Utilization’, vol. 43, p. 1019, Mar. 2012.
[75] V. S. Engelschiøn *et al.*, ‘EAC-1A: A novel large-volume lunar regolith simulant’, *Sci. Rep.*, vol. 10, no. 1, Art. no. 1, Mar. 2020, doi: 10.1038/s41598-020-62312-4.
[76] ‘CLASS Exolith Lab’, *Center for Lunar & Asteroid Surface Science*, Nov. 06, 2020. https://sciences.ucf.edu/class/exolithlab/ (accessed Nov. 06, 2020).
[77] L. Sibille, P. Carpenter, R. Schlagheck, and R. A. French, ‘Lunar Regolith Simulant Materials: Recommendations for Standardization, Production and Usage’, NASA, Technical Publication 20060051776, Sep. 2006. Accessed: Nov. 10, 2020. [Online]. Available: https://ntrs.nasa.gov/citations/20060051776.
[78] P. S. Greenberg, D.-R. Chen, and S. A. Smith, ‘Aerosol measurements of the fine and ultrafine particle content of lunar regolith’, 2007.
[79] Y. Liu, D. W. Schnare, B. C. Eimer, and L. A. Taylor, ‘Dry separation of respirable lunar dust: providing samples for the lunar airborne dust toxicity advisory group’, *Planet. Space Sci.*, vol. 56, no. 11, pp. 1517–1523, 2008.
[80] K. Manick, S.-J. Gill, J. Najorka, M. S. Rumsey, C. L. Smith, and L. Duvet, ‘European Space Agency Exploration Sample Analogue Collection [ESA2C]’, presented at the 49th Lunar and Planetary Science Conference, Texas, USA, Mar. 2018.
[81] CLASS Exolith Lab, ‘LHS-1 Lunar Highlands Simulant’, University of Central Florida, Orlando FL, USA, Fact Sheet, Mar. 2019. Accessed: Nov. 06, 2020. [Online]. Available: https://sciences.ucf.edu/class/exolithlab/.
[82] CLASS Exolith Lab, ‘LMS-1 Lunar Mare Simulant’, University of Central Florida, Orlando FL, USA, Fact Sheet, Mar. 2019. Accessed: Nov. 06, 2020. [Online]. Available: https://sciences.ucf.edu/class/exolithlab/.

[83] L. A. Taylor and Y. Liu, ‘Important considerations for lunar soil simulants’, in *Earth and Space 2010: Engineering, Science, Construction, and Operations in Challenging Environments*, 2010, pp. 106–118.
[84] I. I. I. Carrier W.~D., J. ~K. Mitchell, and A. Mahmood, ‘The relative density of lunar soil’, *Lunar Planet. Sci. Conf. Proc.*, vol. 4, p. 2403, Jan. 1973.
[85] D7481-18ASTM, *Standard test methods for determining loose and tapped bulk densities of powders using a graduated cylinder. ASTM International*. 2018.
[86] A. Meurisse, J. C. Beltzung, M. Kolbe, A. Cowley, and M. Sperl, ‘Influence of Mineral Composition on Sintering Lunar Regolith’, *J. Aerosp. Eng.*, vol. 30, no. 4, Art. no. 4, Jul. 2017, doi: 10.1061/(ASCE)AS.1943-5525.0000721.
[87] X. Chen, Y. Zhang, D. Hui, M. Chen, and Z. Wu, ‘Study of melting properties of basalt based on their mineral components’, *Compos. Part B Eng.*, vol. 116, pp. 53–60, 2017, doi: 10.1016/j.compositesb.2017.02.014.
[88] A. Tsuchiyama and E. Takahashi, ‘Melting kinetics of a plagioclase feldspar’, *Contrib. Mineral. Petrol.*, vol. 84, no. 4, pp. 345–354, 1983, doi: 10.1007/BF01160286.
[89] V. Badescu, Ed., *Moon*. Berlin, Heidelberg: Springer Berlin Heidelberg, 2012.
[90] ‘Chapter Five - Material Characterization for Additive Manufacturing’, p. 43.
[91] X. Zheng *et al.*, ‘Design and optimization of a light-emitting diode projection micro-stereolithography three-dimensional manufacturing system’, *Rev. Sci. Instrum.*, vol. 83, no. 12, Art. no. 12, Dec. 2012, doi: 10.1063/1.4769050.
[92] Z. A. Munir, U. Anselmi-Tamburini, and M. Ohyanagi, ‘The effect of electric field and pressure on the synthesis and consolidation of materials: A review of the spark plasma sintering method’, *J. Mater. Sci.*, vol. 41, no. 3, Art. no. 3, Feb. 2006, doi: 10.1007/s10853-006-6555-2.
[93] X. Zhang *et al.*, ‘Spark plasma sintering of a lunar regolith simulant: Effects of parameters on microstructure evolution, phase transformation, and mechanical properties’, *Ceram. Int.*, 2020.
[94] A. V. Radhamani, H. C. Lau, M. Kamaraj, and S. Ramakrishna, ‘Structural, mechanical and tribological investigations of CNT-316 stainless steel nanocomposites processed via spark plasma sintering’, *Tribol. Int.*, vol. 152, p. 106524, Dec. 2020, doi: 10.1016/j.triboint.2020.106524.
[95] B. A. Obadele, O. S. Adesina, O. P. Oladijo, and E. N. Ogunmuyiwa, ‘Fabrication of functionally graded 316L austenitic and 2205 duplex stainless steels by spark plasma sintering’, *J. Alloys Compd.*, vol. 849, p. 156697, Dec. 2020, doi: 10.1016/j.jallcom.2020.156697.
[96] Y. Long *et al.*, ‘High-strength Ti–6Al–4V with ultrafine-grained structure fabricated by high energy ball milling and spark plasma sintering’, *Mater. Sci. Eng. A*, vol. 585, pp. 408–414, Nov. 2013, doi: 10.1016/j.msea.2013.07.078.
[97] M. Tokita, ‘Large-Size-WC/Co Functionally Graded Materials Fabricated by Spark Plasma Sintering (SPS) Method’, *Materials Science Forum*, 2003. https://www.scientific.net/MSF.423-425.39 (accessed Nov. 14, 2020).
[98] V. K. Balla, L. B. Roberson, G. W. O’Connor, S. Trigwell, S. Bose, and A. Bandyopadhyay, ‘First demonstration on direct laser fabrication of lunar regolith parts’, *Rapid Prototyp. J.*, 2012.
[99] M. Fateri, R. Sottong, M. Kolbe, J. Gamer, M. Sperl, and A. Cowley, ‘Thermal properties of processed lunar regolith simulant’, *Int. J. Appl. Ceram. Technol.*, vol. 16, no. 6, pp. 2419–2428, 2019, doi: https://doi.org/10.1111/ijac.13267.
[100] L. A. Sitta and M. Lavagna, ‘3D PRINTING OF MOON HIGHLANDS REGOLITH SIMULANT’, *Th Int. Astronaut. Congr.*, p. 7, 2018.

[101] B. Sarbandi, ‘Finite element simulation of ceramic deformation during sintering’, p. 126.
[102] M. Liu *et al.*, ‘Digital light processing of lunar regolith structures with high mechanical properties’, *Ceram. Int.*, vol. 45, no. 5, Art. no. 5, Apr. 2019, doi: 10.1016/j.ceramint.2018.12.049.
[103] X. Zhang *et al.*, ‘Microstructure evolution during spark plasma sintering of FJS-1 lunar soil simulant’, *J. Am. Ceram. Soc.*, vol. 103, no. 2, Art. no. 2, Feb. 2020, doi: 10.1111/jace.16808.
[104] Y. Cheng, Z. Cui, L. Cheng, D. Gong, and W. Wang, ‘Effect of particle size on densification of pure magnesium during spark plasma sintering’, *Adv. Powder Technol.*, vol. 28, no. 4, pp. 1129–1135, Apr. 2017, doi: 10.1016/j.apt.2017.01.017.
[105] G. Marnier, C. Keller, J. Noudem, and E. Hug, ‘Functional properties of a spark plasma sintered ultrafine-grained 316L steel’, *Mater. Des.*, vol. 63, pp. 633–640, Nov. 2014, doi: 10.1016/j.matdes.2014.06.053.
[106] K. Crosby, L. Shaw, C. Estournès, G. Chevallier, A. Fliflet, and A. Imam, ‘Enhancement in Ti–6Al–4V sintering via nanostructured powder and spark plasma sintering’, *Powder Metall.*, vol. 57, pp. 147–154, Apr. 2014, doi: 10.1179/1743290113Y.0000000082.
[107] N. Poondla, T. S. Srivatsan, A. Patnaik, and M. Petraroli, ‘A study of the microstructure and hardness of two titanium alloys: Commercially pure and Ti–6Al–4V’, *J. Alloys Compd.*, vol. 486, no. 1, pp. 162–167, Nov. 2009, doi: 10.1016/j.jallcom.2009.06.172.
[108] C. Keller, K. Tabalaiev, G. Marnier, J. Noudem, X. Sauvage, and E. Hug, ‘Influence of spark plasma sintering conditions on the sintering and functional properties of an ultra-fine grained 316L stainless steel obtained from ball-milled powder’, *Mater. Sci. Eng. A*, vol. 665, pp. 125–134, May 2016, doi: 10.1016/j.msea.2016.04.039.
[109] C. S. Ray, S. T. Reis, S. Sen, and J. S. O’Dell, ‘JSC-1A lunar soil simulant: Characterization, glass formation, and selected glass properties’, *J. Non-Cryst. Solids*, vol. 356, no. 44, pp. 2369–2374, Oct. 2010, doi: 10.1016/j.jnoncrysol.2010.04.049.
[110] K. Karami *et al.*, ‘Continuous and pulsed selective laser melting of Ti6Al4V lattice structures: Effect of post-processing on microstructural anisotropy and fatigue behaviour’, *Addit. Manuf.*, vol. 36, p. 101433, Dec. 2020, doi: 10.1016/j.addma.2020.101433.
[111] M. Yakout, ‘A study of the relationship between thermal expansion and residual stresses in selective laser melting of Ti-6Al-4V’, *J. Manuf. Process.*, p. 13, 2020.
[112] D. C. Hofmann *et al.*, ‘Compositionally graded metals: A new frontier of additive manufacturing’, *J. Mater. Res.*, vol. 29, no. 17, pp. 1899–1910, 2014, doi: 10.1557/jmr.2014.208.
[113] N. Oxman, S. Keating, and E. Tsai, ‘Functionally graded rapid prototyping’, *Innov. Dev. Virtual Phys. Prototyp.*, pp. 483–489, 2012, doi: 10.1201/b11341-78.
[114] J. Schleppi, J. Gibbons, A. Groetsch, J. Buckman, A. Cowley, and N. Bennett, ‘Manufacture of glass and mirrors from lunar regolith simulant’, *J. Mater. Sci.*, vol. 54, no. 5, pp. 3726–3747, Mar. 2019, doi: 10.1007/s10853-018-3101-y.

[115] B. A. Lomax, ‘Characterisation and evaluation of lunar regolith simulants for use in in-situ resource utilisation research’, *Submitt. Degree Master Sci. Inst. Mech. Process Energy Eng. Heriot-Watt Univ.*, p. 54, 2018.
[116] G. M. Brown, A. Peckett, C. H. Emeleus, R. Phillips, and R. H. Pinsent, ‘Petrology and mineralogy of Apollo 17 mare basalts’, vol. 6, pp. 1–13, 1975.
[117] P. Nieke, J. Kita, M. Häming, and R. Moos, ‘Manufacturing dense thick films of lunar regolith simulant EAC-1 at room temperature’, *Materials*, vol. 12, no. 3, p. 487, 2019, doi: 10.3390/ma12030487.